Appendix 1. Climate

Contents

Figures

Appendix 1. Climate

Satellite rainfall estimates were used as a key input to an energy-balance model for simulation of snowpack accumulation and depletion. The NOAAs Climate Prediction Center (CPC) provides gridded precipitation estimates at 0.1 degree resolution (RFE 2.0) that blend satellite and station observations using geostatistical methods (Xie and Arkin, 1997). Satellite inputs include thermal infrared imagery from geostationary weather satellites, typically acquired every 30 minutes, and passive microwave imagery acquired several times a day by polar orbiting satellites. The thermal infrared data provide a measure of cloud-top temperatures, which are correlated with the occurrence of rainfall. The microwave imagery detects upwelling radiation that has been scattered by the presence of precipitation-sized ice particles in the cloud layer. Station data are accessed through the Global Telecommunication System (GTS) of the World Meteorological Organization (WMO). These are a relatively small subset of rainfall station data collected by the national meteorological services of United Nations (UN) member countries. (Theoretically, over 4,000 stations are part of the GTS reporting network in the Central Asian RFE domain, but on any given day, only about 500 stations report. No station data from within Afghanistan are entered into the GTS. Only surface observations from neighboring countries are available to reduce bias in the RFE 2.0 estimates for Central Asia.) Precipitation estimates from thermal infrared imagery and microwave imagery are blended using weights that are inversely proportional to the error of each type of imagery. Then interpolated station data are used to remove bias from the blended satellite rainfall estimate field, while retaining its shape and form. NOAA/CPC has produced precipitation estimates of 24-hour accumulations for Afghanistan operationally each day since 2003.

A distributed version of the Utah Energy Balance Accumulation and Melt Model (UEB) (Tarboton, 1994; Tarboton and others, 1995) was used for the study. The snow water equivalent (SWE) model is a spatially distributed snowmelt model driven with remotely sensed and assimilated meteorological data. The UEB uses a lumped representation of the snowpack with two primary state variables, namely water equivalence (or total amount of water, expressed in depth (mm), in the snowpack), and energy content relative to a reference state of water in the ice phase at 0˚C. This version of the model runs in a spatially distributed mode using a grid resolution of 10 km. The UEB uses physically based calculations of the radiative, sensible, latent, and advective heat exchanges (i.e., exchanges, or fluxes, of energy resulting from incoming and outgoing short- and long-wave radiation, thermal or heat conduction, evaporation and condensation, and horizontal heat transport). An equilibrium parameterization of snow-surface temperature accounts for differences between snow-surface temperature and average snowpack temperature, without having to introduce additional state variables. Melt outflow is a function of the liquid fraction and is parameterized according to Darcy's law. This parameterization allows the model to account for continued outflow even when the energy balance is negative. It was not possible to carry out snowmelt model parameter calibration for Afghanistan because of the lack of direct observational data. Instead, parameters from the calibration of Tarboton and Luce (1996) using data from the Central Sierra Snow Laboratory were used.

The UEB was forced using RFE 2.0 precipitation and output fields from two operational atmospheric models: NOAAs Global Data Assimilation System (GDAS) and the Air Force Weather Agencys MM5. GDAS provided radiation fields, and the MM5 provided surface air temperature, wind, humidity, and atmospheric pressure. The six-hourly meteorological variable fields were downscaled to match the 0.1 degree resolution of the RFE 2.0 using the USGS GTOPO30 digital elevation database. The GTOPO30 is a global topographic data set (Gesch and others, 1999) with a spatial resolution of 30 arcseconds (about 1 km), well suited to downscaling the GDAS (1.0 degree, about 100 km) and MM5 (45 km) fields to the 0.1 degree grid used for the UEB. The MODIS Snow Cover Daily L3 Global (MOD10A1) data set (Hall and others, 2000), at 500-m resolution, was compared with the UEB simulated snow-cover extent for Afghanistan as a check on model performance. (MODIS snow-cover data are distributed by the National Snow and Ice Data Center (NSIDC) DAAC in Boulder, Colo.)

The UEB produced daily national grids of snow-water equivalent (SWE) at 0.1 degree resolution (fig. 1-1) for the period October 1, 2002, through August 24, 2007, characterizing five winter seasons. Basin areas above the Tang-i-Gharu streamgage on the Kabul River and the Shukhi streamgage on the Panjsher River were delineated from GTOPO30 using ArcGIS. These polygons were used to produce daily values of total snow-water volume above each of the two streamgages for the five winter seasons.

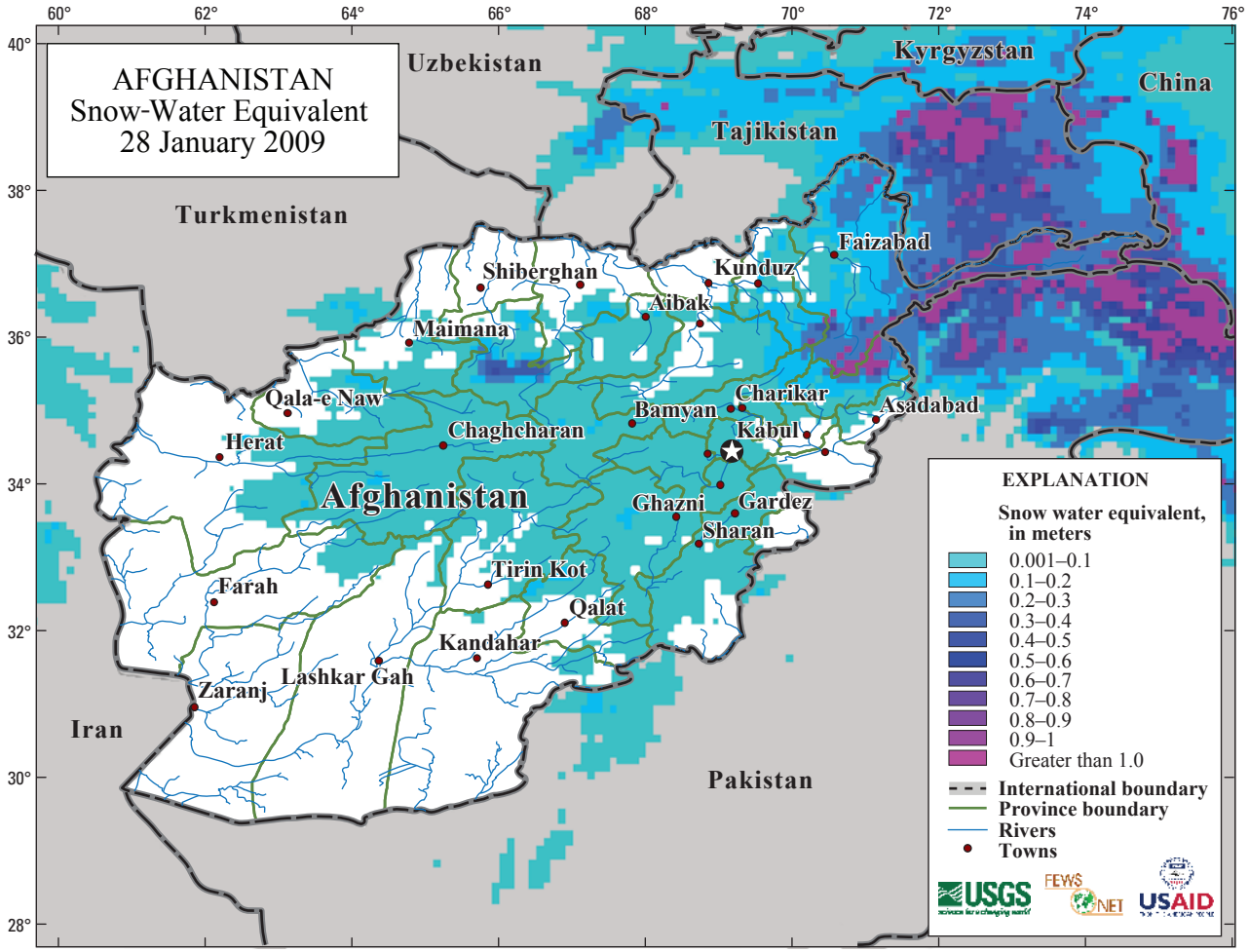

Base Map from Afghanistan Information Management Service (AIMS).
Map produced by the USGS/EROS Data Center. Snow ablation model:
USGS FEWS NET. http://earlywarning.usgs.gov/Afghan/snowwater.php

Figure 1-1. Daily national snow-water equivalent grid produced with the Utah Energy Balance Accumulation and Melt Model (Tarboton and Luce, 1996) at 0.1 degree resolution.

References Cited

Gesch, D.B., Verdin, K.L., and Greenlee, S.K., 1999, New land surface digital elevation model covers the Earth: EOS, Transactions of the American Geophysical Union, v. 80, no. 6, pp. 69–70, online at http://edcdaac.usgs.gov/gtopo30/gtopo30.html

Hall, D.K., Riggs, G.A., and Salomonson, V.V., 2000, updated daily, MODIS/Terra Snow Cover Daily L3 Global 500m Grid V004, January to March 2003: Boulder, Colo., U.S.A., National Snow and Ice Data Center, Digital media.

Tarboton, D.G., 1994, Measurement and modeling of snow energy balance and sublimation from snow, *in* Proceedings, International Snow Science Workshop, Snowbird, Utah, October 31 to November 2, Utah Water Research Laboratory working paper no. WP-94-HWR-DGT/002.

Tarboton, D.G., Chowdhury, T.G., and Jackson, T.H., 1995, A spatially distributed energy balance snowmelt model, *in* Biogeochemistry of seasonally snow-covered catchments, Tonnessen, K.A., and others, eds.: Proceedings of a Boulder Symposium, July 3–14, IAHS Publ. no. 228, p. 141–155.

Tarboton, D.G., and Luce, C.H., 1996, Utah Energy Balance Snow Accumulation and Melt Model (UEB)—Computer model technical description and users guide: Utah Water Research Laboratory and USDA Forest Service Intermountain Research Station.

Xie, P., and Arkin, P.A., 1997, A 17-year monthly analysis based on gauge observations, satellite estimates, and numerical model outputs: Bulletin of the American Meteorological Society, v. 78(11), p. 2539–58.

This page intentionally left blank.

Appendix 2. Geomorphology Methods

Contents

Figures

Appendix 2. Geomorphology Methods

Advanced Spaceborne Thermal Emission and Reflection Radiometer (ASTER) measures reflected radiation in three bands between 0.520 and 0.860 µm (visible-near-infrared region–VNIR) and in six bands from 1.00 to 2.43 µm (short-wave infrared region–SWIR), with 15-m and 30-m spatial resolution, respectively (Fujisada, 1995). In addition, ASTER measures emitted thermal radiation in five bands in the 8.125- to 11.650-µm wavelength region (thermal-infrared–TIR) at 90-m resolution (Fujisada, 1995). Standard ASTER data products (VNIR-SWIR reflectance, TIR emissivity, and TIR decorrelation stretch products) and (or) their equivalents were used in this study. For example, a false-color composite image of ASTER bands 6, 3, and 1, displayed as red, green, and blue, respectively, is shown in figure 2-1A. This image represents a mosaic of three ASTER scenes from a single 60-km wide orbital swath, which covers more than 95 percent of the Kabul Basin and MODFLOW study area, and was acquired on October 12, 2001. Similar to a Landsat TM 7-4-2 color composite, vegetation appears green and dominates the land-use/cover pattern of much of the northernmost Shomali subbasin, which is irrigated and intensively cultivated using a one-crop per year rotation system. Basin-fill alluvial sediments reflect a bright white color in this ASTER band combination and notably dominate the Deh Sabz subbasin; built-up and impervious areas of Kabul and its suburbs appear dark blue and dominate the Paghman and Upper Kabul and Central Kabul subbasin. Eolian materials and hardpans (e.g., ferricrete, calcrete, and (or) silcrete) appear variously colored, but the former displays recognizable dune and wind-streak patterns in the visible ASTER bands for areas east of the Barik Ab tributary of the Panjsher River in the northeastern portions of the Shomali subbasin dominated by rangeland and pasture land-use types, bare soils, and rock outcrops.

A mosaic of three decorrelation stretch images of ASTER TIR bands 13, 12, and 10, displayed as red, green, and blue, respectively, is shown in figure 2-1B. Because ASTER decorrelation images distributed by the Eros Data Center are "standard products" generated on a scene-by-scene basis, histogram matching was done in order to facilitate generation of a "seamless" mosaic along this single orbital swath of ASTER data. However, the high degree of compositional variability in the northern portion of the Shomali subbasin created statistical problems in effectively matching brightness values between overlapping areas within the upper and middle ASTER scenes. This problem produced a notable seam that only affects the basin-fill alluvial areas of the Shomali subbasin, but not the surrounding bedrock and vegetated areas (fig. 2-1B). Decorrelation stretch images are used to enhance the brightness variations between TIR bands related to compositional differences in emissivity, while suppressing correlated inter-channel brightness related to variations in radiant temperature (Gillespie and others, 1986). In this case, compositional variations are due largely to relative abundances of silica-rich minerals (mostly quartz), which appear red, mafic minerals (e.g., pyroxenes and amphiboles), which appear blue, and carbonate minerals and vegetation, both of which appear green. Mixed colors are largely the result of mixtures between these three basic mineral types. For example, purple areas dominate alluvial fans derived from mafic-rock source areas in the western portions of the Shomali subbasin (fig. 2-1B) because these rocks tend to weather more rapidly to produce clay- and ferric-iron rich soils that are commonly enriched in residual silica (Kahle and others, 1988). Notably, such color variations displayed in TIR decorrelation stretch imagery can be used to determine relative ages, assuming constant rates of weathering (Kahle and others, 1988). The rates of weathering in a high-desert environment such as Afghanistan are likely to be too slow and on geologic time scales to impact the chloride concentrations in groundwater.

Chlorophyll-bearing vegetated areas have been masked out of the decorrelation stretch image on the basis of a thresholded band-ratio image of ASTER VNIR bands 3/2; thus, these areas appear black (fig. 2-1B). Although this is an effective method for masking green vegetation and built-up urban areas, which typically contain mixtures of impervious surfaces and green vegetation (Ridd, 1995), this band ratio is ineffective for mapping dry vegetation with little or no chlorophyll. Therefore, dry vegetation and carbonate minerals can be confused if spectral mapping is based solely on ASTER SWIR or TIR data alone. However, carbonate minerals yield stronger absorption features in ASTER SWIR band 8 and ASTER TIR band 14 than dry vegetation containing lignin and cellulose (Murphy, 1995), which allows for the use of band-ratios and relative band-depth images with conservative thresholds as a solution in order to emphasize areas of highest abundance and probability of occurrence for carbonate minerals (Murphy, 1995).

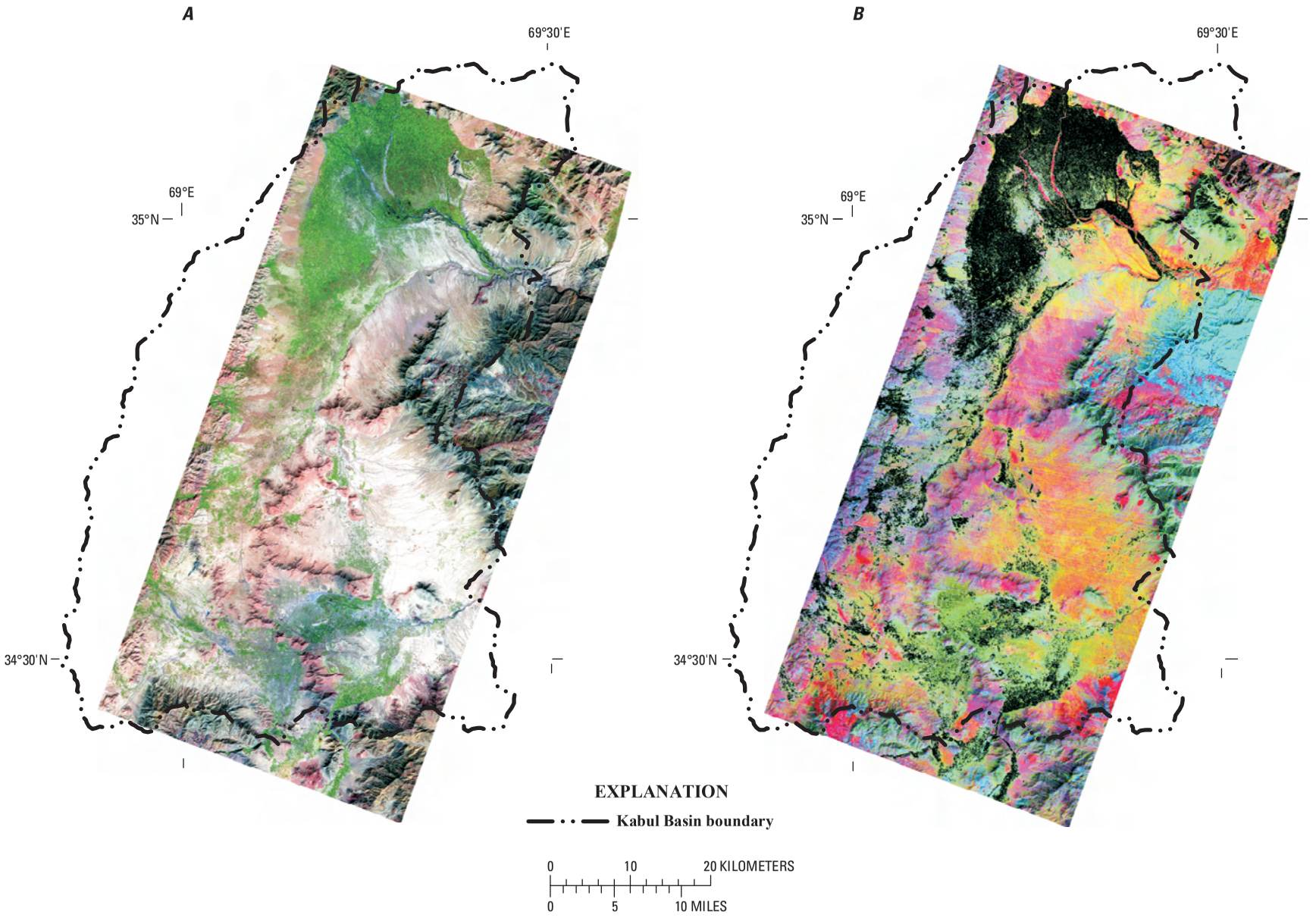

Figure 2-1. (A) False-color composite of ASTER bands 6, 3, and 1 displayed as red, green, and blue, respectively; and (B) a mosaic of three decorrelation stretch images of ASTER TIR bands 13, 12, and 10 displayed as red, green, and blue, respectively, for the Kabul Basin, Afghanistan.

References Cited

Fujisada, H., 1995, Design and performance of ASTER instrument: Proceedings of SPIE, the International Society for Optical Engineering, v. 2583, p. 16–25.

Gillespie, A.R., Kahle, A.B., and Walker, R.E., 1986, Color enhancement of highly correlated images—I. Decorrelation and HIS contrast stretches: Remote Sensing of Environment, v. 20, p. 209–235.

Kahle, A.B., Gillespie, A.R., Abbott, E.A., Abrams, M.J., Walker, R.E., and Gordon, H., 1988, Relative dating of Hawaiian lava flows using multispectral thermal infrared images—A new tool for geologic mapping of young volcanic terranes: Journal of Geophysical Research, v. 93, no. B12, p. 15239–15251.

Murphy, R.J., 1995, The effects of surficial vegetation cover on mineral absorption feature parameters: International Journal of Remote Sensing, v. 16, no. 12, p. 2153–2164.

Ridd, M.K., 1995, Exploring a V-I-S (vegetation-impervious surface-soil) model for urban ecosystem analysis through remote sensing—Comparative anatomy for cities: International Journal of Remote Sensing, v. 16, no. 12, p. 2165–2185.

Appendix 3. Surface Water

Contents

Figures

Tables

Appendix 3. Surface Water

Böckh (1971) provides streamflow data for eight streamgages in the vicinity of the city of Kabul for the 1963 water year (fig. 3-1, tables 3-1 through 3-7). This information is reproduced here to make it available and to illustrate the importance of stream and aquifer interactions in the Kabul Basin. Böckh (1971) used streamflow data to evaluate the gains and losses to the rivers between the selected streamgages. Streamgages 1 and 2 are on the Kabul River as the river enters the city of Kabul from the south. Streamgages 3 and 4 are on the Logar River southeast of the city of Kabul and just before the Logar River enters the Kabul River. Streamgages 5, 6, 7, and 8 are on the Qargha (Karga) and Paghman Rivers just west of the city of Kabul.

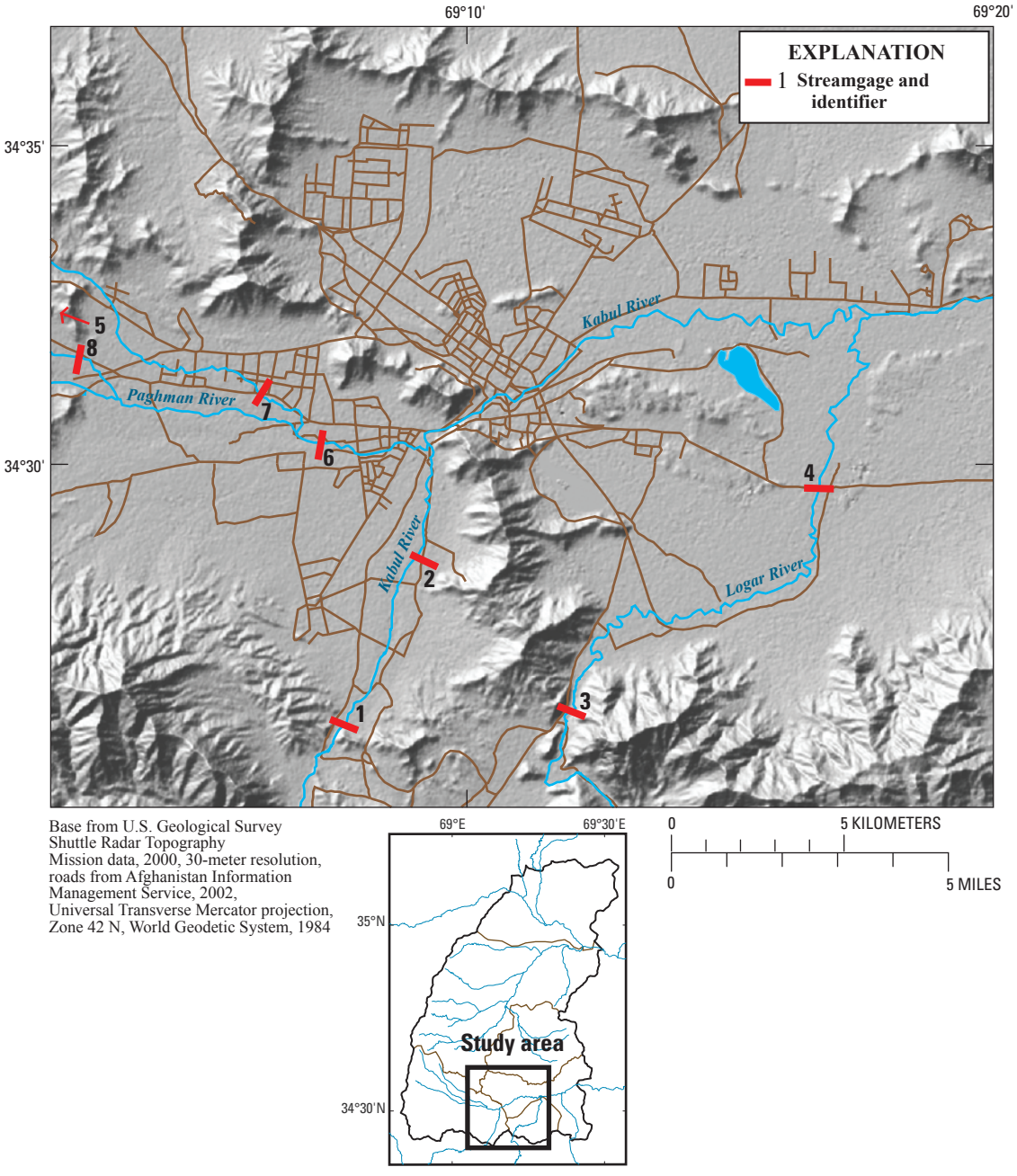

Figure 3-1. Location of streamgages at which runoff and water losses are provided by Böckh (1971). Streamgage numbers and locations are based on map plates from Böckh (1971).

Table 3-1. Discharge between streamgages 1 and 2.

[See figure 3-1 (modified from Böckh,1971)]

Year	Month	Discharge, in cubic meters per second		
		Streamgage 1	Streamgage 2	Water gain or loss (-)
1962	October	0.65	[1]0.26	0.39
	November	1.17	[1]0.35	0.82
	December	1.84	0.74	1.10
1963	January	2.81	1.59	1.22
	February	2.07	1.09	0.98
	March	1.70	0.75	0.95
	April	6.55	5.20	1.35
	May	22.50	17.20	5.30
	June	6.56	5.05	1.51
	July	0.64	0.26	0.38
	August	0.59	0.17	0.42
	September	0.51	0.18	0.33
Annual mean		3.97	2.74	1.23

[1] Computed from discharge at Streamgage 1.

Table 3-2. Annual discharges and losses for streamgages 1 and 2, 1963 water year.

[See figure 3-1 (modified from Böckh, 1971). Maximum runoff (river plus channels) is 45.5 cubic meters per second May 15 and 19, 1963. Minimum runoff (river plus channels) is 0.34 cubic meter per second August 17, 1963]

	Discharge, in millions of cubic meters		
	Streamgage 1	Streamgage 2	Water loss
River	96.5	71.1	25.4
Channels	27.5	14.3	13.2
Total discharge	124.0	85.4	38.6

Table 3-3. Discharge differences between streamgages 1 and 2 for selected periods.

[See figure 3-1 (modified from Böckh, 1971)]

Periods	Discharge, in cubic meters per second					
	Streamgage 1		Streamgage 2		Water loss	
	River	Channel	River	Channel	River	Channel
April - June	10.70	1.20	8.41	0.73	2.29	0.47
July - November	0.08	0.63	0.00	0.25	0.08	0.38
December - March	1.15	0.97	0.42	0.63	0.73	0.34
Annual Mean	3.10	0.87	2.25	0.49	0.85	0.38

Table 3-4. Discharge between streamgages 3 and 4.

[See figure 3-1 (modified from Böckh, 1971)]

Year	Month	Discharage, in cubic meters per second		
		Streamgage 3	Streamgage 4	Water gain or loss (-)
1962	October	5.78	[1]4.58	-1.20
	November	12.00	[1]12.5	0.50
	December	15.80	[1]16.7	0.90
1963	January	16.00	17.60	1.60
	February	14.80	16.00	1.20
	March	12.90	13.90	1.00
	April	8.40	7.85	-0.55
	May	20.50	21.40	0.90
	June	2.11	0.57	-1.54
	July	1.89	[1]0.55	-1.34
	August	1.62	[1]0.41	-1.21
	September	1.78	[1]0.39	-1.39
Annual mean		9.47	9.37	-0.10

[1] Discharge diverted to the Kabul River was added.

Table 3-5. Annual discharges and losses for streamgages 3 and 4, 1963 water year.

[See figure 3-1 (modified from Böckh, 1971). Maximum runoff (river plus channels) is 50.0 cubic meters per second May 13, 1963. Minimum runoff (river plus channels) is 1.50 cubic meters per second September 8, 1963.]

	Discharge, in millions of cubic meters		
	Streamgage 3	Streamgage 4	Water loss
River	231.8	227.0	4.8
Channels	67.7	65.5	2.2
Total discharge	299.5	292.5	7.0

Table 3-6. Discharge differences between streamgages 3 and 4 for selected periods.

[See figure 3-1 (modified from Böckh, 1971)]

Periods	Discharge, in cubic meters per second					
	Streamgage 3		Streamgage 4		Water gain or loss (-)	
	River	Channel	River	Channel	River	Channel
October - November	5.94	2.95	6.90	1.64	0.96	-1.31
December - March	13.30	1.60	12.80	3.30	-0.50	1.70
April - May	11.80	2.60	11.00	3.60	-0.80	1.00
June - September	0.15	1.70	0.18	0.30	0.03	-1.40
Annual mean	7.43	2.04	7.28	2.09	-0.15	0.05

Table 3-7. Discharge between streamgages 5, 7, and 8, and 6.

[See figure 3-1 (modified from Böckh, 1971); --, no data]

Year	Month	Discharge, in cubic meters per second					
		Streamgage 5[1]	Streamgage 7[2]	Streamgage 8[3]	Sum of streamgage 5, 7, and 8	Streamgage 6[4]	Water gain or loss (-)
1962	October	0.03	0.00	0.00	0.03	0.00	-0.03
	November	0.03	0.00	0.00	0.03	0.01	-0.02
	December	0.03	0.00	0.00	0.03	0.29	0.26
1963	January	0.04	0.13	0.00	0.17	0.37	0.02
	February	0.04	0.11	--	0.15	0.15	0.00
	March	0.02	0.05	1.12	0.19	0.22	0.03
	April	0.10	0.00	1.06	1.16	0.67	-0.49
	May	1.92	0.26	3.61	5.79	3.77	-2.02
	June	0.37	0.00	0.06	0.43	0.07	-0.36
	July	0.19	0.00	0.05	0.24	0.01	-0.23
	August	0.10	0.00	0.02	0.12	0.00	-0.11
	September	0.05	0.00	0.02	0.08	0.01	-0.08
Annual mean		0.24	0.05	0.41	0.70	0.46	-0.24

[1] Paghman River plus channel.

[2] Qargha (Karga) River.

[3] Cheltan River plus channel.

[4] Paghman River which is downstream of streamgages 5, 7, and 8.

References Cited

Böckh, E.G., 1971, Report on the groundwater resources of the city of Kabul, report for Bundesanstalt für Geowissenschaften und Rohstoffe [unpublished]: BGR file number 0021016, 43 p.

Appendix 4. Chemical and Isotopic Analysis of Air and Water Samples

Contents

Appendix 4. Chemical and Isotopic Analysis of Air and Water Samples

Chemical and isotopic data collected for this investigation included measurements of (1) the stable hydrogen and oxygen isotopic composition of surface water and groundwater, (2) the major and minor-element chemical composition (30 elements) of surface water and groundwater, (3) the dissolved gas compositions of surface water and groundwater including dissolved nitrogen, argon, carbon dioxide, oxygen, methane, helium, and the chlorofluorocarbons (CFCs, CFC-11, CFC-12, and CFC-113), (4) the chlorofluorocarbon composition of air samples, and (5) the tritium content of surface water and groundwater.

Air Samples

Ambient air samples were collected in 500-cc stainless steel vessels that were evacuated in the laboratory and opened at the collection site. The valves were then closed, and the vessels were returned to the U.S. Geological Survey (USGS) Reston Chlorofluorocarbon Laboratory for analysis. Two separate vessels were filled at each site, and each vessel was analyzed in duplicate by gas chromatography with an electron-capture detector (see *http://water.usgs.gov/lab/cfc*); laboratory precision was approximately 5 percent.

Water Chemistry

Samples for cation analysis were collected in acid-rinsed 250-mL polyethylene bottles. The samples were filtered in the lab and acidified with 2 mL of Ultrex nitric acid. The samples for anion analysis were filtered and collected in 250-mL polypropylene containers. The containers were obtained from the USGS Water Quality Laboratory.

Major cations and silica were analyzed at the USGS Water Chemistry Laboratory in Reston, Va., using the Perkin-Elmer Optima DV 4300, a dual view inductively coupled plasma optical atomic emission spectrometer (ICP-OES). The detection limits for mass concentrations of Ca, Mg, SiO_2, Na, and K by ICP-OES were less than 0.05, 0.05, 0.1, 0.05, and 0.1 mg/L, respectively. Precision for measurements of Ca, Mg, SiO_2, Na, and K mass concentrations by ICP-OES was 1 to 3 percent.

Trace cations were analyzed using a Perkin Elmer ELAN6000 inductively coupled plasma mass spectrometer (ICP-MS) with a Scott-type cross-flow nebulizer for sample introduction and a quadrupole mass separator. The detection limits for mass concentrations of As, Ba, Cu, Mo, Ni, Rb, Sb, and V were 0.1 µg/L. The detection limits for mass concentrations of Al, Cr, Li, Mn, Se, Sr, and Zn were 1 µg/L. The detection limits for mass concentrations of Cd, Pb, and U were 0.05 µg/L. The detection limits for mass concentrations of B and Fe were 0.02 µg/L. Precision was generally 1 to 3 percent for all elements analyzed by ICP-MS.

A Dionex series DX-120 equipped with Dionex AS14 (analytical) and AG-14 (guard) columns was used for the analysis of fluoride, chloride, bromide, nitrate, and sulfate. Detection limits for mass concentrations of chloride, sulfate, nitrate, bromide, and fluoride were less than 0.2, 0.2, 0.1, 0.05, and 0.05 mg/L, respectively. The precision for measurements of chloride, sulfate, nitrate, and bromide was 1 to 3 percent. The precision for measurements of fluoride was 3 to 5 percent.

Alkalinity was measured in the USGS Water Chemistry Laboratory using a Radiometer TIM900 titration manager and ABU93 autoburette. Some bicarbonate may have been lost between the time the samples were collected and when they were analyzed in the laboratory, as was evidenced by calcium carbonate precipitates in some sample bottles collected in 2006 (samples from karez 10 and 69, spring 67 and 181, and well 28, 33, 42, 47, 172, 203, and 208). For these, alkalinity was estimated using a charge-balance algorithm. The mass concentration detection limit of bicarbonate for alkalinity titrations was 2 mg/L. The precision for alkalinity titrations was approximately 1 percent.

Major Dissolved Gases

Water samples for analysis of major dissolved gases were collected in 150-cc septum bottles without headspace. Mass concentrations of N2, Ar, O2, CO2, and CH4 were measured in the USGS Dissolved Gas Laboratory, Reston, Va., using gas-chromatographic procedures (*http://water.usgs.gov/lab/cfc/*). Replicate analyses of N2 and Ar in laboratory standards prepared by equilibrating water samples with air were typically within 1 percent and yielded calculated equilibration temperatures within ± 0.5°C. The dissolved O2 and CO2 analyses have uncertainties similar to those of dissolved N2 and Ar but can deviate as much as 20 percent between replicate samples because of varying extents of microbiological processes occurring in the sample bottles after collection and during storage prior to analysis.

Dissolved Helium-4

Water samples for analysis of dissolved helium were collected in 150-cc septum bottles without headspace, in a manner identical to the collection of samples for major dissolved gases. Samples were analyzed at the USGS Dissolved Gas Laboratory, Reston, Va., using a gas-chromatographic procedure (http://water.usgs.gov/lab/cfc/) that also determines the volume concentrations, σ, of dissolved hydrogen (H_2) and neon (Ne). The precisions of the analyses were 5–10, 10–20, and 10 percent for He, Ne, and H_2, respectively.

Chlorofluorocarbons

Water samples for CFC analysis were collected in 250-mL cap glass bottles with foil-lined caps (*http://water.usgs.gov/lab/cfc*). A closed path using copper tubing was established between the well or spring and the bottom of the bottle. The bottle was submersed in a bucket of source water and allowed to overflow several volumes before capping under water, without headspace. The caps were taped, and the bottles were returned to the USGS for analysis. Mass fractions of the CFCs, CFC-11 (trichlorofluoromethane, CFCl3), CFC-12 (dichlorodifluoromethane, CF2Cl2), and CFC-113, (trichlorotrifluoroethane, C2F3Cl3), were determined at the USGS Chlorofluorocarbon Laboratory, Reston, Va., using purge and trap gas chromatography with an electron-capture detector (Busenberg and Plummer, 1992; http://water.usgs.gov/lab/cfc/). The CFC mass fractions were calibrated to average air compositions measured at Niwot Ridge, Colo. (Climate Monitoring and Diagnostics Laboratory (CMDL) of the National Oceanic and Atmospheric Administration (NOAA), U.S. Department of Commerce (*http://www.cmdl.noaa.gov/*)). The detection limit for CFC-11 and CFC-12 mass fractions was near 0.3 picograms per kilogram of water (pg/kg) and approximately 1.0 pg/kg for CFC-113.

Tritium

Water samples for ^{3}H analysis were collected in 500-cc plastic bottles. The bottles were sealed with screw caps with conical liners. Approximately 10 cc of air space was left in the bottles during filling to accommodate expansion on warming. The samples were enriched electrolytically and analyzed by liquid scintillation counting in the low-level ^{3}H laboratory of the USGS, Menlo Park, Calif., following procedures modified from those described by Thatcher and others (1977).

Stable Hydrogen and Oxygen Isotopes

The relative stable isotope-amount ratio of hydrogen, $\delta^{2}H$, is defined according to the relation

$$\delta^{2}\mathrm{H} = \frac{N\left(^{2}\mathrm{H}\right)_{\mathrm{B}} \Big/ N\left(^{1}\mathrm{H}\right)_{\mathrm{B}} - N\left(^{2}\mathrm{H}\right)_{\mathrm{B}} \Big/ N\left(^{1}\mathrm{H}\right)_{\mathrm{B}}}{N\left(^{2}\mathrm{H}\right)_{\mathrm{VSMOW}} \Big/ N\left(^{1}\mathrm{H}\right)_{\mathrm{VSMOW}}}, \quad (1)$$

where $N(^{2}H)_{B}/N(^{1}H)_{B}$ and $N(^{2}H)_{VSMOW}/N(^{1}H)_{VSMOW}$ are the ratios of the isotopes ^{2}H and ^{1}H of hydrogen in unknown water B and the international measurement standard VSMOW. The hydrogen isotopic composition is reported on a scale such that the 10^{3} $\delta^{2}H$ value of SLAP reference water is -428 exactly (Gonfiantini, 1978). For stable oxygen isotopes, $\delta^{18}O$ is defined according to the relation

$$\delta^{18}\mathrm{O} = \frac{N\left(^{18}\mathrm{O}\right)_{\mathrm{B}} \Big/ N\left(^{16}\mathrm{O}\right)_{\mathrm{B}} - N\left(^{18}\mathrm{O}\right)_{\mathrm{VSMOW}} \Big/ N\left(^{16}\mathrm{O}\right)_{\mathrm{VSMOW}}}{N\left(^{18}\mathrm{O}\right)_{\mathrm{VSMOW}} \Big/ N\left(^{16}\mathrm{O}\right)_{\mathrm{VSMOW}}}, \quad (2)$$

where $N(^{18}O)_{B}/N(^{16}O)_{B}$ and $N(^{18}O)_{VSMOW}/N(^{16}O)_{VSMOW}$ are the ratios of the number of isotopes ^{18}O and ^{16}O of oxygen in unknown water B and the international measurement standard VSMOW. The oxygen isotopic composition is reported on a scale such that the 10^{3} $\delta^{18}O$ value of SLAP reference water is -55.5 exactly (Gonfiantini, 1978).

Water samples for determination of the stable isotopic composition of oxygen and hydrogen were untreated and collected in 60-cc glass bottles with Polyseal liner caps. For determination of $\delta^{2}H$ values, water samples were analyzed using gaseous hydrogen equilibration (Coplen and others, 1991). The 2-σ precision of 10^{3} $\delta^{2}H$ values is better than 2. For determination of $\delta^{18}O$ values, water samples are analyzed using the carbon dioxide-water equilibration technique of Epstein and Mayeda (1953). The 2-σ precision of 10^{3} $\delta^{18}O$ values is better than 0.2.

References Cited

Busenberg, E., and Plummer, L.N., 1992, Use of chlorofluorocarbons (CCl_3F and CCl_2F_2) as hydrologic tracers and age-dating tools: Example—The alluvium and terrace system of central Oklahoma: Water Resources Research, v. 28, no. 9, p. 2257–2284.

Coplen, T.B., Wildman, J.D., and Chen, J., 1991, Improvements in the gaseous hydrogen-water equilibration technique for hydrogen isotope ratio analysis: *Analytical Chemistry*, v. 63, p. 910–912.

Epstein, S., and Mayeda, T., 1953, Variation of O^{-18} content of water from natural sources: *Geochim. Cosmochim. Acta* 4, p. 213–224.

Gonfiantini, R., 1978, Standards for stable isotope measurements in natural compounds: *Nature*, v. 271, p. 534–536.

Thatcher, L.L., Janzer, V.J., and Edwards, K.W., 1977, Methods for determination of radioactive substances in water and fluvial sediments: U.S. Geological Survey Techniques of Water-Resources Investigations of the United States Geological Survey, chap. 5, book 5, Laboratory Analysis, p. 67–71, and p. 79–81, 1962, The distribution of tritium fallout in precipitation over North America: *International Association of Scientific Hydrology* VII, no. 2, p. 48–58.

This page intentionally left blank.

Appendix 5. Agricultural Water Use

Contents

Figures

Appendix 5. Agricultural Water Use

A simplified surface energy balance (SSEB) method (Senay and others, 2007), described below, was used to estimate crop water use in the Kabul Basin. Global 1-degree reference ET (ETo), based on 6-hourly GDAS output, is calculated daily at USGS EROS on an operational basis (Verdin and Klaver, 2002; Senay and Verdin, 2003). The GDAS ETo uses the standard Penman-Monteith equation as outlined in the FAO publication by Allen and others (1998). The feasibility of using the GDAS ETo for such applications was recommended by Senay and Verdin (2005) after a comparison with station-based daily ETo showed encouraging results with r^2 values exceeding 0.9. Daily global reference ET values were available for all days between 2001 and 2006. For 2000, the daily reference ET values were not complete. For the missing time periods, the average reference ET from 2001 to 2005 was used.

Prior to using these data, a downscaling of the GDAS 1-degree results was performed to produce 10km GDAS reference ET data sets. The approach utilized the International Water Management Institute (IWMI) historical (1961–90) potential ET. The IWMI data set is originally a 16km spatial resolution that has been disaggregated to 10km. The downscaling technique utilized the 10km IWMI data to create a fractional relation, on a per-pixel basis, between each 10km IWMI pixel (x) and the corresponding 100km IWMI pixel (y) value (artificially created to match the 100km GDAS). This fractional relation could then be applied back to the 100km GDAS pixels to downscale these data to a spatial resolution of 10km:

$$x / y * GDAS$$

The result was a times series of daily fields of maximum potential ET at all locations (grid cells) in the study area, in units of millimeters per day.

The next step in the SSEB method uses remote sensing of land-surface properties to make estimates of actual ET fractions, which in most locations are less than the full potential amount defined by an ideal cover type (short grass) transpiring at a rate that fully meets atmospheric demand (ETo).

Image data acquired by the Moderate Resolution Imaging Spectroradiometer (MODIS) instrument on the NASA Terra satellite were used to measure land-surface temperature and vegetative cover. The MODIS instrument provides 36 spectral bands, including 16 in the thermal portion of the spectrum. Thermal surface measurements were collected from the MODIS 8-day Land Surface Temperature/Emissivity (LST/E) product (MOD11A2). The LST/E images provide per-pixel temperature and emissivity values at 1-km spatial resolution for the 8-day composite product. Temperatures are extracted in degrees Kelvin with a view-angle dependent algorithm applied to direct observations. This study utilized measurements of average daytime land-surface temperature for 8-day composite periods throughout the growing season. More than twenty 8-day periods beginning in early April through the end of October were processed for each year in the period 2001–2006.

MODIS Vegetation Index (VI) products use reflectance measures in the red (620–670 nm), near infrared (841–876 nm), and blue (459–479 nm) bands to provide spectral measures of vegetation vigor. The MODIS VI products include the standard normalized difference vegetation index (NDVI) and the enhanced vegetation index (EVI). Both indices are available at 250-m, 500-m, and 1-km spatial resolution. The primary difference between the two indices is that EVI uses blue reflectance to provide better sensitivity in high biomass regions. Because this study was concentrated on irrigated agriculture in an otherwise dry land environment, the standard 16-day NDVI product at 250-m resolution was used for this analysis. Images from the Landsat ETM+ and ASTER instruments were also used to define irrigated agricultural areas of interest in the Kabul Basin.

MODIS LST and NDVI data are distributed by the Land Processes Distributed Active Archive Center DAAC), located at the USGS EROS Center in Sioux Falls, S. Dak., as are the Landsat and ASTER images.

Full energy balance solutions with remote sensing (Allen and others, 2005; Bastiaanssen and others, 1998) assume that the temperature difference between the land surface and the air (near-surface temperature difference) varies linearly with land-surface temperature. This linear relation is used to estimate variations in the sensible heat flux. The technique is based on the use of two anchor pixels, *hot* and *cold*, representing dry and bare agricultural fields, in the first case, and wet, well-vegetated fields in the second. It assumes that the *hot* pixel experiences no latent heat, i.e., ET = 0.0, whereas the *cold* pixel achieves maximum potential ET. In the SSEB approach, this assumption is extended such that the latent heat flux (actual evapotranspiration) also varies linearly between the *hot* and *cold* pixels. While the *hot* pixel of a bare agricultural area experiences little ET, and the *cold* pixel of a well-watered irrigated field experiences maximum ET, the remaining pixels in the study area will experience ET in proportion to their land-surface temperature in the range defined by the *hot* and *cold* pixels (fig. 5-1).

The study focused on two major expanses of irrigation in the Kabul Basin, an extensive area north of Kabul in the Panjsher Valley and a narrower band of irrigation along the Kabul River south of the city. The northern area was sub-divided into two sections to minimize the effects of elevation differences on measurements of surface temperature. For each of the three areas, a polygon was defined around the irrigated fields by interpreting a combination of Landsat, ASTER, and MODIS images. The irrigated areas consist of both well-vegetated and sparsely vegetated areas, with some arid/semi-arid areas at the periphery.

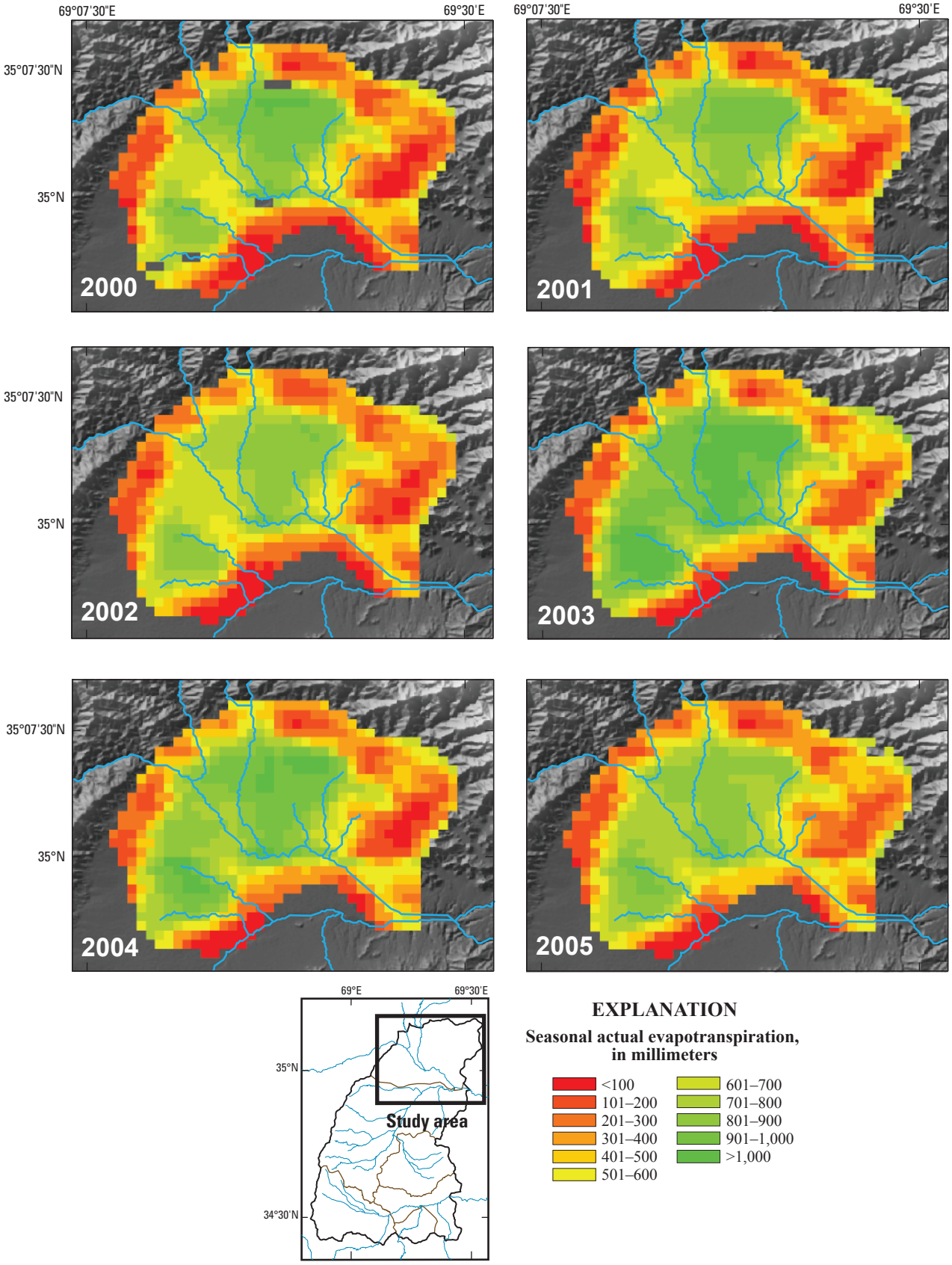

Figure 5-1. Estimates of seasonal actual evapotanspiration for irrigated lands above Shukhi streamgage on the Panjsher River.

Within each of the three areas, sets of three *hot* and three *cold* pixels were selected for each 8-day composite period for each growing season. An average of the three pixels was used to establish the reference *hot* and *cold* values throughout the study area. For each time period, cold pixels representing well-vegetated and well-watered crops were selected on the basis of a combination of low LST values and high MODIS NDVI values. Similarly, hot pixels, representing low-density vegetation and dry land, were identified by high LST values and very low NDVI values.

Values of land-surface temperature for each of the six pixels (three *hot*, three *cold*) were extracted using ArcGIS software. The resulting database files were imported into an Excel spreadsheet where average *hot* and *cold* pixel values were calculated.

The reference temperatures of the *hot* and *cold* pixels were used to calculate proportional fractions of ET on a per-pixel basis. The ET fraction (ETfrac) was calculated for each pixel by applying the following equation to each of the 8-day MODIS land-surface-temperature grids:

$$\mathrm{ETfrac} = \frac{\mathrm{TH} - \mathrm{Tx}}{\mathrm{TH} - \mathrm{TC}}, \quad (1)$$

where TH is the reference temperature from the *hot* pixels selected for a given scene; TC is the reference temperature of the *cold* pixels selected for that scene; and Tx is the land-surface temperature for any given pixel in the 8-day composite scene.

The ETfrac formula was applied to all the 8-day growing season composites for each year (fig. 5-2), resulting in a series of more than 25 images per season. The ETfrac images were used in conjunction with reference ET grids to calculate the per-pixel actual ET values for each scene. Daily reference ET images were averaged over 8-day periods to match the MODIS LST composite periods. The calculation of actual ET (ETact) was achieved using the following formula:

$$\mathrm{ETact} = \mathrm{ETfrac} * \mathrm{ETref}, \quad (2)$$

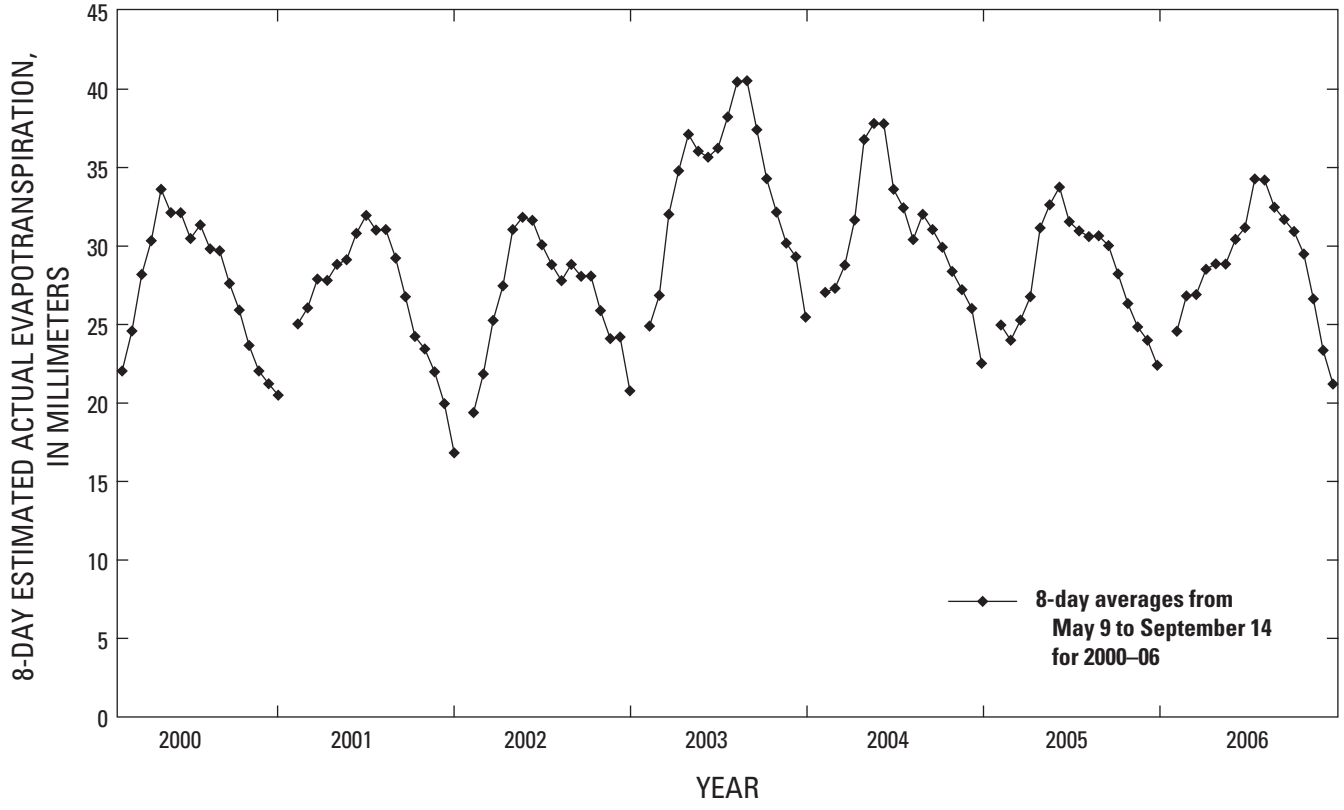

Figure 5-2. Seasonal traces of 8-day values of estimated actual evapotanspiration for irrigated lands above Shukhi streamgage on the Panjsher River.

This SSEB approach allowed for use of estimates of reference ET, at a coarse spatial resolution, to derive spatially distributed ET measurements on the basis of the variability of land-surface temperature at 1-kilometer resolution (fig. 7). Actual crop ET for the 7-year period, 2000–2006, was used to assess the quality of each growing season in the Kabul study areas. Polygons delineating irrigated crop areas were used with actual 1-km gridded ET values (fig. 7) to calculate spatially aggregated actual ET for each season, permitting preparation of seasonal traces of actual ET (fig. 5-2).

Water use was also estimated at small, scattered irrigated fields outside the three polygons modeled with the SSEB where, because of the relatively coarse spatial resolution of the 1-km MODIS thermal data, the SSEB could not be applied. In an effort to extrapolate findings for major irrigated areas to these smaller parcels, a regression equation was developed between seasonal ETa and MODIS seasonal maximum NDVI at a spatial resolution of 250 m. Only those pixels with seasonal maximum NDVI greater than or equal to 0.35 were used. To reduce data noise, the seasonal ETa values were averaged within NDVI classes at 0.05 increments from 0.35 to 0.8 using 2005 data from the Kabul 1 irrigation area (fig. 5-1). The resulting regression equation (seasonal ETa verses maximum NDVI) was reliable in that more than 90 percent of the spatial variability in seasonal ETa was explained by maximum NDVI. The regression equation was applied to the seasonal maximum NDVI data for each year to estimate seasonal ETa for small discontinuous areas of irrigation.

References Cited

Allen, R.G., Pereira, L., Raes, D., and Smith, M., 1998, Crop evapotranspiration—Food and Agriculture Organization of the United Nations: Rome, Italy, ISBN 92-5-104219-5, 290 p.

Bastiaanssen, W.G.M., Menenti, M., Feddes, R.A., and Holtslag, A.A.M., 1998, A remote sensing surface energy balance algorithm for land (SEBAL): (1) Formulation. Journal of Hydrology, 212 (213): p. 213–229.

Senay, G.B., and Verdin, J.P., 2003, Characterization of yield reduction in Ethiopia using a GIS-based crop water balance model: Canadian Journal of Remote Sensing, v. 29(6), p. 687–692.

Senay, G.B., and Verdin, J.P., 2005, Evaluating reference evapotranspiration (ETo) model output from the Global Data Assimilation System using station ETo in the U.S.: Proceedings of Reclamation ET workshop: State-of-the-art review of ET remote sensing science and technology, February 8–10, Fort Collins, Colo.

Senay, G.B., Buddy, M., Verdin, J.P., and Melesse, A.M., 2007, A coupled remote sensing and simplified surface energy balance approach to estimate actual evapotranspiration from irrigated fields: Sensors, v. 7, p. 979–1000.

Verdin, J., and Klaver, R., 2002, Grid cell based crop water accounting for the famine early warning system: Hydrological Processes, v. 16, p. 1617–1630.

This page intentionally left blank.

Appendix 6. Conceptual Model Development

Contents

Table

Appendix 6. Conceptual Model Development

The Kabul Basin is in a "basin and range" setting, approximately 10 to 35 km wide and about 80 km long, where the valley is filled with quaternary and tertiary sediments and the ranges are composed of uplifted crystalline and sedimentary rocks (Bohannon and Turner, 2007). The generalized valley section (fig. 3) provides a general profile of the basin where Quaternary sediments are typically less than 80 m thick in the valley, the underlying tertiary (Neogene) sediments are as much as 1,000 m thick (Homilius, 1969), and the sediments are surrounded by primarily crystalline bedrock that forms the valley walls and basin boundaries.

The model was aligned with the primary axis of the basin where the lateral model boundary coincides with the major drainage divides forming the mountains that define the valley. The model was simulated with a horizontal cell size of 400 by 400 m in the row and column direction. The model was subdivided vertically into four layers (fig. 8) representing the major hydrogeologic units indicated in the generalized section shown in figure 3. The top-most model-cell elevations were interpreted from 30-m Digital Elevation Model (DEM) land-surface elevations averaged for each model cell. Model-layer thicknesses and extent address both hydrogeologic and numerical considerations and are discussed below. The model design used in this study was similar to that used by Pool and Dickinson (2007) for a regional groundwater flow simulation at the southwestern United States and northern Mexico border with similar geohydrologic characteristics.

Model layer 1 represents Quaternary and recent sediments in the valley-bottom, subbasin areas (fig. 8). To avoid dewatering model cells, layer 1 was not extended laterally up the hillsides where sediments may often be unsaturated. The thickness of layer 1 varies with location and was estimated using several sources of data. Drilling logs were obtained from records maintained by Afghanistan Geological Survey (AGS) (Amin Akbari, written commun., 2007) and (Eng. Hassan Safi, (Danish Committee for Aid to Afghan Refugees, written commun., 2007). A few hundred drilling records were concentrated in the developed areas of the city of Kabul, about 20 records were in the Shomali Plain near the center of the valley, and drilling records were fewer in the lateral margins of the model. Where available, drilling logs that indicated the depth to the top of Neogene (assumed to be the top of conglomerate sediments) were used to estimate the Neogene top elevation. In areas with no other information, recently dug or driven wells with no associated log information were used to indicate a minimum thickness of quaternary sediments. The depth to the Neogene in the model, which comprises the thickness of quaternary and recent sediments in model layer 1, was generally 30 to 60 m. Quaternary sediment thicknesses of just over 100 m were observed, and modeled, in some areas, primarily toward the centers of the subbasins.

Model layers 2 and 3 follow the elevation of the bottom of model layer 1, with the exception of hillsides, and each layer was 500 m thick (fig. 8). On hillsides, model layer 4 was the topmost model layer (fig. 8) and represented the mapped surficial geology (fig. 2), which was primarily bedrock. In the valley bottoms of the subbasin areas (fig. 1), Neogene sediments were assumed to be present beneath Quaternary and recent unconsolidated deposits (fig. 2). The Neogene and mapped consolidated rocks were extended through model layers 2 and 3 and were represented as an upper unit in layer 2 and a lower unit in layer 3. To roughly approximate basins that narrow with depth, the lateral extent of Neogene sediments in model layer 3 were assumed to be a few hundred meters closer to each basin center than in model layer 2 (fig. 8). Model layer 4 was designed to represent basal bedrock with a thickness of 1,000 m (fig. 3).

Boundary Conditions and Stresses

Boundary conditions and stresses were simulated using various MODFLOW-2000 model packages (Harbaugh and others, 2000) designed to represent components of the hydrologic system. River leakage and flow accumulation was simulated using the stream-flow routing (SFR1) package (Prudic and others, 2004). The rates of fluxes into or out of the model were estimated using results of various components of the investigation discussed in the report under Surface-Water Flow and Chemical and Isotopic Data. Stresses in the aquifer system include recharge, streamflow discharge, and domestic and agricultural water use. Recharge in the system includes direct infiltration of precipitation, leakage from the major rivers flowing through the basin (fig. 1), leakage from tributary perennial streams that drain adjacent upland areas (fig. 1), and lateral groundwater inflows from upland areas not drained by perennial streams (fig. 8). Recharge to the basin aquifers was from river leakage, leakage in irrigated areas, and from direct infiltration during the winter months.

Hydraulic Properties

The surficial and bedrock geology of the Kabul Basin was fairly well known and has recently been reinterpreted by Bohannon and Turner (2007) and Lindsay and others (2005). Geologic maps were used to assign zones of similar hydraulic properties in the conceptual model. The geology was grouped into eight major hydrogeologic zones (fig. 3) on the basis of general hydraulic conductivity and storage characteristics (table 6-1). The categories were Quaternary fan alluvium and colluvium (sand and gravel) (K1); river channel sediments (K2); loess (K3); unconsolidated conglomerates (K4); upper (K5) and lower (K6) Neogene sediments consisting of semi-consolidated fine-grained sediments and gravel; sedimentary rocks including sandstone, siltstone, limestone, and dolomite (K7); and all metamorphic and igneous rocks (K8). The hydraulic properties of the primary unconsolidated aquifer

sediments in the Kabul Valley are generally high, on the order of 10s of meters per day. Hydraulic characteristics of the Quaternary and recent sediments (table 6-1) have been determined from aquifer tests (Böckh, 1971) and have been evaluated in other investigations (Houben and Tunnermeier, 2005; Niard, 2007).

The geohydrologic parameter categories used in the model were based on general hydraulic characteristics of sediments or rocks. The hydraulic properties of the secondary aquifers, for example various consolidated bedrocks, are generally orders of magnitude lower, than the unconsolidated (primary) aquifer sediments, and can be approximated for the purposes of a regional investigation from values reported in the literature (Freeze and Cherry, table 2.2, 1979) for similar materials. Although some zones contain geologic materials with distinctly different origin or nature, for the purpose of the conceptual model, they have relatively similar hydraulic properties and are grouped together (table 6-1). For example, sedimentary rocks and metamorphic and igneous rocks are grouped into two geohydrologic parameter zones, K7 and K8, respectively. These rocks contain numerous subunits with varying lithologic characteristics; however, the hydraulic conductivity and storage properties for these rocks are orders of magnitude lower than those for the other unconsolidated or partially consolidated rocks represented by the more permeable hydrogeologic zones (K1–K6). In regional groundwater flow systems, the simulated flow is typically less sensitive to low hydraulic-conductivity parameter zones than the higher hydraulic-conductivity parameter zones because much more groundwater is transmitted in the more permeable zones than in the less permeable zones.

Faults in the Kabul Basin are areas where the bedrock is likely to be highly fractured resulting in greater water-storage and transmitting capabilities. A number of fault systems, particularly the Sorubi-Konar fault system to the east and the Chaman-Paghman fault system to the west (Ruleman and others, 2007), are associated with the mountain ranges that define the Kabul Basin (fig. 3). Photolinear features (lineaments) in the Kabul Basin hillsides and ridges, observed by this investigation using LANDSAT imagery, were also considered to be possible fracture zones. Faults and lineaments were assumed to be fracture zones with hydraulic conductivity and porosity greater than the surrounding rock. Fracture zones were simulated in bedrock aquifers in model layers 2–4, by buffering mapped features by approximately 250 m, to ensure that they were represented by at least one model cell width were present, and were represented by a hydraulic conductivity and porosity an order of magnitude greater than the surrounding bulk rock properties (table 6-1).

Table 6-1. Model parameters and generalized hydraulic characteristics of sediment and rock aquifers in the Kabul Basin, Afghanistan.

[m/d, meters per day; – not known or available]

Sediment or rock unit	Hydraulic conductivity (m/d[1])	Geologic codes[2]	Conceptual model					
			Model layer(s)	Horizontal hydraulic conductivity (m/d)	Parameter code	Vertical hydraulic conductivity (m/d)	Parameter code	Porosity[3]
Fan alluvium and colluvium	–	Q_{34}ac	1	50	K1	5	K1v	0.28
River channel sediments	388.8	Q_4a	1	100	K2	10	K2v	0.3
Loess	34.56	Q_3loe	1	20	K3	2	K3v	0.28
Unconsolidated conglomerates	–	Q_3a	1	3	K4	0.3	K4v	0.28
Upper Neogene	8.64	N_2cgs	1,2	1	K5	0.1	K5v	0.1
Lower Neogene	–	N_2cgs	3	3	K6	0.3	K6v	0.1
Sedimentary rocks	–	all sedimentary rock codes	4	0.1	K7	0.1	K7v	0.01
Metamorphic and igneous rocks[4]	–	all metamorphic and igneous codes	4	0.01	K8	0.01	K8v	0.01

[1] Reported by Böckh (1971).

[2] Bohannon and Turner (2007) and Linsay and others (2005) shown on figures 3 and 8.

[3] Porosity used in flowpath analysis only.

[4] In areas of known or suspected fracturing or faulting the hydraulic conductivity was 0.1 m/d and porostiy was 0.05.

References Cited

Böckh, E.G., 1971, Report on the groundwater resources of the city of Kabul, report for Bundesanstalt für Geowissenschaften und Rohstoffe [unpublished]: BGR file number 0021016, 43 p.

Bohannon, R.G., and Turner, K.J., 2007, Geologic map of quadrangle 3468, Chak Wardak-Syahgerd (509) and Kabul (510) quadrangles, Afghanistan: U.S. Geological Survey Open-File Report 2005–1107–A. 1 sheet.

Freeze, R.A., and Cherry, J.A., 1979, Groundwater: Englewood Cliffs, N.J., Prentice-Hall, 604 p.

Harbaugh, A.W., Banta, E.R., Hill, M.C., and McDonald, M.G., 2000, MODFLOW-2000, the U.S. Geological Survey modular groundwater-flow model—User guide to modularization concepts and the groundwater flow process: U.S. Geological Survey Open-File Report 00 -92, 121 p.

Homilius, Joachim, 1969, Geoelectrical investigations in east Afghanistan, Geophysical Prospecting, v. 17, issue 4, p. 468-487.

Houben, Georg, and Tunnermeier, Torge, 2005, Hydrogeology of the Kabul Basin, Part I—Geology, aquifer characteristics, climate and hydrology: Federal Institute for Geosciences and Natural Resources (BGR), Hannover, Germany, p. 45.

Lindsay, C.R., Snee, L.W., Bohannon, R.R., Wahl, R.R., and Sawyer, D.A., comps., 2005, Geologic map of quadrangle 3568, Polekhomri (503) and Charikar (504) quadrangles, Afghanistan: U.S. Geological Survey Open-File Report 2005-1101-A, 1 sheet.

Pool, D.R., and Dickinson, J.E., 2007, Groundwater flow model for the Sierra Vista Subwatershed and Sonoran portions of the Upper San Pedro Basin, southeastern Arizona, United States, and northern Sonora, Mexico: U.S. Geological Survey Scientific Investigations Report 2006–5228, 48 p.

Prudic, D.E., Konikow, L.F., and Banta, E.R., 2004, A new streamflow routing (SFR1) package to simulate stream-aquifer interaction with MODFLOW-2000: U.S. Geological Survey Open-File Report 2004–1042, 95 p.

Ruleman, C.A., Crone, A.J., Machette, M.N., Haller, K.M., and Rukstales, K.S., 2007, Map and database of probable and possible Quaternary faults in Afghanistan: U.S. Geological Survey Open-File Report 2007–1103, 39 p., 1 pl.

Appendix 7. Geomorphology and Composition of Basin-Fill Sediments

Contents

Figures

Appendix 7. Geomorphology and Composition of Basin-Fill Sediments

ASTER VNIR-SWIR reflectance and TIR decorrelation stretch imagery are shown in figures 2-1A and 2-1B, respectively. The TIR decorrelation stretch image (fig. 2-1B) broadly shows mixtures of rocks and basin sediments containing silicic, carbonate, and mafic minerals. For example, green-colored areas most abundant in carbonate minerals correspond with the Central Kabul and Paghman and Upper Kabul subbasin (fig. 2-1B). These subbasins are dominated by impervious cover and building materials in and around the city of Kabul, which are predominantly made from imported and (or) locally derived sources of limestone and marble building materials. Other notable areas of green-displayed carbonate-bearing minerals are alluvial fans and their limestone and marble source areas on the outer margins of the Dez Sabz subbasin, eastern parts of the Central Kabul subbasin, and southern margins of the Paghman and Upper Kabul subbasin (fig. 2-1B).

Orange and yellow areas may represent various mixtures of quartz-rich alluvium with either dry vegetation or carbonates in either alluvial or hardpan (caliche/calcrete) forms. These colors dominate the central portions of the Dez Sabz subbasin and the eastern half of the Central Kabul subbasin within our image coverage (fig. 2-1B). Surprisingly, cyan colors associated with weathered and ferric-oxidized ultramafic rock source areas to the northeast of the Kabul Basin study area (fig. 2-1B) do not appear in any of the basin alluvial sediments derived from these source areas. One possible explanation is that the rate of weathering of minerals characteristic of ultramafic rocks (e.g., olivine) exceeds the rate of erosion from these areas by catastrophic stream floods.

The most quartz-abundant areas appear bright red and correspond with the flood plains of major stream channels and eolian deposits characterized earlier in the paragraph describing photogeologic interpretation of the VNIR-SWIR imagery (fig. 2-1A). However, visual inspection of image spectra extracted from the latter areas in the corresponding TIR emissivity and VNIR-SWIR reflectance imagery suggests that these eolian deposits are not pure quartz sands but contain mixtures of clay, and perhaps even feldspar minerals. As a result, further analysis of the ASTER TIR and VNIR-SWIR data sets were conducted using several different band-ratios and relative band-depth images to highlight abundances of various minerals and mineral groups on the basis of their characteristic absorption features (Rowan and Mars, 2003; Rowan and others, 2005; Ninomiya and others, 2005; and Hewson and others, 2005), as well as matched-filter processing designed to partially unmix "target" foreground spectral endmembers from their composite "mixed" backgrounds (Harsanyi and Chang, 1994). The result of the latter processing yields images showing the relative abundances of each of the "relatively pure" spectral endmembers, which in this case were derived from the imagery and represent individual minerals, lithologic rock types, mineral-bearing soils, and other types of intimate mixtures of minerals.

Figure 7-1 summarizes the results of several band-ratio and relative absorption band-depth analyses, useful for showing abundances of different mineral types within the basin-fill sediments and surrounding bedrock source areas. In particular for TIR bands, these generally agree with the distribution of carbonate, mafic, and silicic minerals than the green, blue, and red components, respectively, of the decorrelation stretch image shown in figure 2-1B, though the former provides much clearer details on the spatial distribution of these minerals throughout the Kabul Basin. For example, carbonate minerals such as calcite and dolomite yield high brightness values in the ratio of TIR bands 13/14, for which green and (or) dry vegetation do not. Areas with the highest brightness values in this band-ratio appear white (fig. 7-1A) and correspond mainly to carbonate bedrock source areas (e.g., limestones and marbles). However, the red-colored areas suggest less-abundant amounts of carbonate minerals associated with either alluvium derived from these source areas, residual hardpans (e.g., calcrete/caliche) related to fluctuations in the groundwater table, or both. No attempts were made to mask out either the vegetation or the urban-built materials derived mainly from carbonate-rock source materials (fig. 7-1A), and stripping is due to coherent noise in these two bands, which was first noted in similar carbonate mineral mapping work done by Rowan and Mars (2003).

The Dez Sabz subbasin is dominated by carbonate minerals within basin-fill alluvium (fig. 7-1A), as suggested by the noticeable erosion and drainage pattern derived mainly from carbonate-abundant source rocks to the east. On the other hand, lack of carbonate bedrock source areas in the highlands to the west of the Kabul Basin (Bohannon and Turner, 2007) suggest that the Shomali subbasin and westernmost Paghman and Upper Kabul subbasin are dominated by carbonate minerals of the hardpan type rather than carbonate-rock alluvium (fig. 7-1A). Much of the carbonate mineral abundant areas of the easternmost Paghman and Upper Kabul, westernmost Central Kabul, and northernmost portions of the Logar subbasin appear to be related to impervious urban building materials made from carbonates (e.g., limestone/marble dimension stones, cement, and carbonate-rock dominated crushed stone and gravel), though carbonate bedrock sources do occur in areas to the south of these three subbasin (white-colored areas–fig. 7-1A). The areas with the least abundant amounts of carbonate minerals correspond with eolian deposits, which dominate the northeastern portion of the Shomali subbasin, and much of the surrounding bedrock source areas that contain mostly crystalline and siliciclastic bedrock types (fig. 7-1A). In sum, the eastern half of the Kabul Basin appears to be dominated by alluvial carbonate sources, and the western half of the basin appears to be dominated by hardpan carbonate sources (fig. 7-1B), though both types are likely to occur together in varying proportions throughout all of the five subbasins.

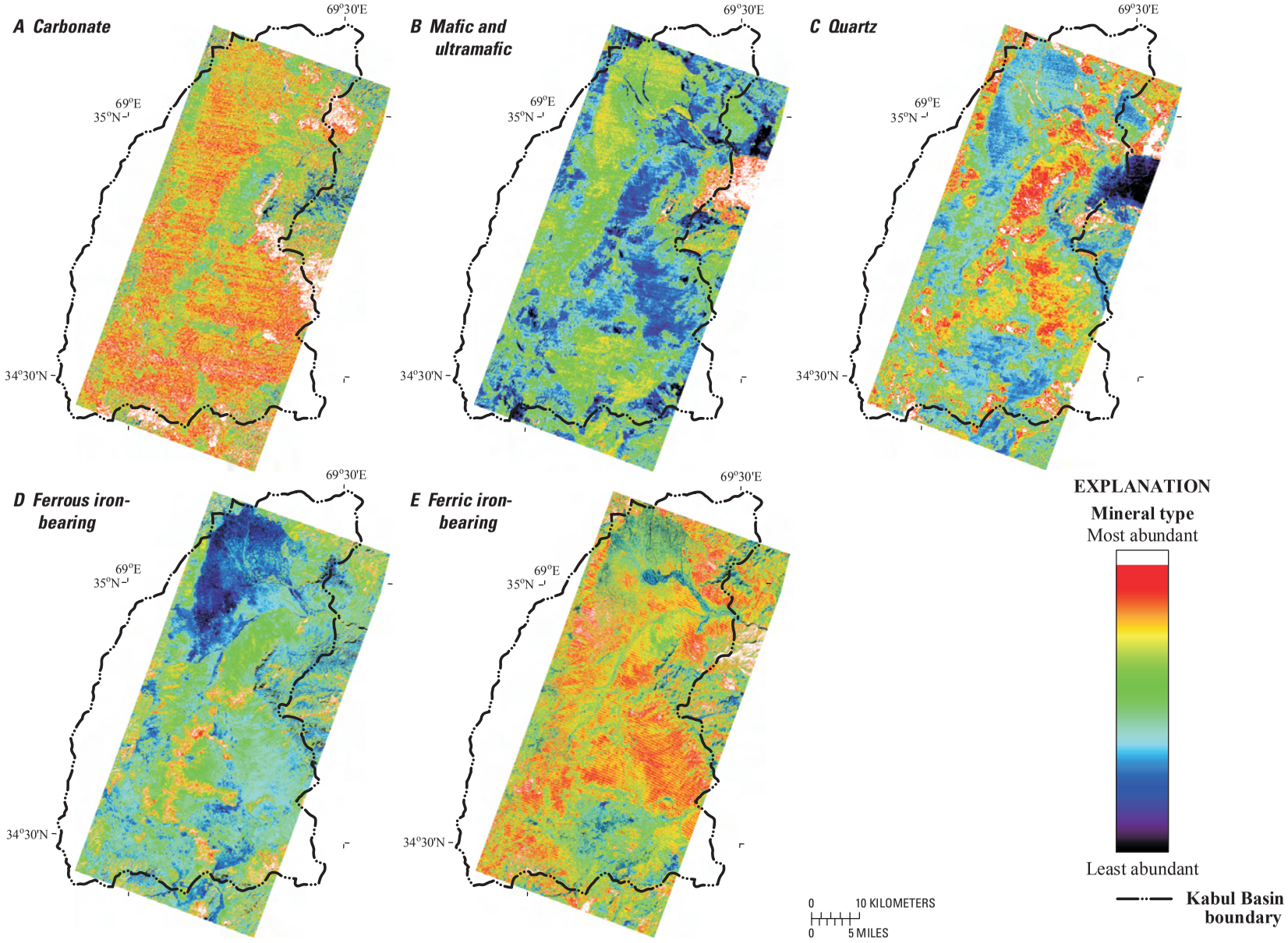

Figure 7-1. ASTER analysis of relative abundance of mineral groups containing (A) carbonate, (B) mafic and ultramafic minerals, (C) quartz, (D) ferrous iron, and (E) ferric iron in the Kabul Basin, Afghanistan. (This figure is the same as figure 11 on page 24 in the report).

Figure 7-1B shows a relative band-depth (RBD) image of TIR bands (12+14)/(13*2) (also referred to as RBD13–Rowan and others, 2005), which highlights the distribution of rocks and sediments containing abundant mafic minerals such as olivine, pyroxene and (or) amphiboles. Mafic mineral areas appear to be lacking throughout much of the Kabul Basin, with areas corresponding to the ultramafic complex northeast of the basin described previously, containing the most abundant levels of these minerals (white- and red-colored areas, fig. 7-1B). Notably, this large area appears distinctly cyan-colored in the decorrelation stretch image (fig. 2-1B). The fact that basin-fill sediments lack the spectral signatures of mafic and ultramafic rock source areas in the surrounding mountains suggest that these minerals do not survive the weathering process and are instead easily converted to other mineral phases such as ferric-iron, clays, and silica. Areas with yellow-colored abundant levels are mostly the result of noise between band 13 and neighboring bands 12 and 14, for areas covered with dense vegetation that were not masked (fig. 7-1B).

The quartz abundance map (fig. 7-1C) is based on the ratio of TIR bands 13/12 and yields a spatial distribution pattern that mimicks the inverse of that of the mafic rock abundance map (fig. 7-1B). This is not surprising because fresh mafic and ultramafic rocks contain little or no quartz, other than residual silica derived from weathering (Kahle and others, 1988). The areas most abundant in quartz appear white-colored (fig. 7-1C) and correspond with Pliocene clastic and Quaternary detrital sediments (mostly sandstone, gravel and loess deposits) northeast of the modern Kabul basin (Bohannon and Turner, 2007). The distribution of quartz in modern-day Kabul basin-fill sediments (red-colored areas–fig. 7-1C) are indicative of the degree of weathering and residual-soil development on alluvial fans and pediments, as well as the amount of alluvial and eolian transport from quartz-rich rocks such as granites, grano-diorites, sandstones, conglomerates, and quartzites surrounding the basin. The Dez Sabz subbasin and the westernmost areas of the Shomali subbasin (fig. 7-1C) contain abundant quartz that appears to be first type (i.e., residual quartz derived from in-situ chemical weathering of alluvial-fan material). This is based on the bedrock geology of the respective source areas, which are predominantly mafic gneisses to the west of the Shomali basin and mafic gneisses and carbonates surrounding the Dez Sabz (Bohannon and Turner, 2007). The northeastern portion of the Shomali subbasin is dominated by quartz of the second type that appears to be eolian in origin and mixed with other minerals as discussed earlier (fig. 7-1C).

The distribution of ferrous- and ferric-iron bearing minerals are shown in figures 7-1D and 11E, respectively. The distribution of ferrous-iron bearing minerals (fig. 7-1D) is based on the ratio sum of ASTER VNIR-SWIR bands (1/2) + (5/3), which resolves the slope of major ferrous absorption features near 1.0 μm, displayed by mafic minerals such as olivine, pyroxene, amphibole, serpentine, biotite, and chlorite (Rowan and others, 2005). The distribution of ferric iron bearing minerals, such as hematite and goethite, were resolved using the ratio of bands 2/1 (fig. 7-1E). With the exception of a few areas, perhaps exposing fresh and least-weathered rocks, most of the bedrock source areas containing quartz-poor ultramafic rocks (fig. 7-1C) appear to contain more abundant ferric-iron minerals (white areas, fig. 7-1E) than ferrous-iron minerals (red and white areas, fig. 7-1D), most likely the result of extensive weathering over time. Other areas displaying abundant ferrous-iron minerals correspond to bedrock and youngest alluvial fan and talus material derived from biotite- and amphibole-bearing gneiss source areas surrounding the basin (Bohannon and Turner, 2007). Notably, the basin sediments are depleted in ferrous-iron minerals (fig. 7-1D), because of their higher susceptibility to weathering as noted previously. However, transported and residual forms of ferric-iron (i.e., alluvial and hardpan) appear to dominate all of the subbasin of the Kabul Basin (red-colored areas, fig. 7-1E), except for the city of Kabul and surrounding suburbs that are dominated by urban/impervious land-cover materials, typically derived from carbonate rock sources. Indeed, many areas containing abundant ferric-iron, perhaps in hardpan form such as ferricrete, also contains abundant carbonate minerals in the form of calcrete (compare fig. 7-1A with fig. 7-1E).

Other stable and (or) residual mineral phases with greater degrees of resistance to chemical weathering, such as clay and mica minerals, were mapped using spectral endmembers identified within the VNIR-SWIR reflectance, followed by matched-filter processing as described earlier. In this case, VNIR-SWIR spectral endmembers representing pixels dominated by clay- and mica-minerals and TIR spectral endmembers representing feldspar-minerals and (or) intermediate-composition volcanic rocks were chosen on the basis of a principal component analysis and pixel purity index analysis described by Green and others (1988) and Boardman and others (1995), respectively. TIR spectral endmembers representing feldspar-bearing deposits, were mapped using the spectral angle mapper (SAM) algorithm described by Kruse and others (1993). SAM outputs images showing the similarity in spectral shape between image spectra and reference spectral endmembers, which can be used as a measure of abundance of any particular spectral endmember from pixel to pixel.

The area containing the most abundant distribution of feldspar minerals on the basis of the TIR emissivity data is the eolian deposits within the northeastern portion of the Shomali subbasin (fig. 7-2A). Notably, clay- and feldspar-rich rocks both exhibit lower band 11 emissivity and higher band 12 emissivity than rocks and sediments containing higher proportions of quartz (Rowan and others, 2005). However, in this case, VNIR-SWIR analysis suggests that clay abundances are relatively low throughout much of these eolian deposits as compared to other parts of the Kabul Basin dominated by alluvial basin-fill sediments (yellow- and green-colored smectite abundant levels, fig. 7-2B), which suggests that they are comprised mostly of mixtures of quartz (fig. 7-1C), feldspars (fig. 7-2A), and ferric-iron (fig. 7-1E) with only minor amounts of clays (fig. 7-2B) and carbonates (fig. 7-1A). Other notable areas of high feldspar abundances include felsic-gneiss bedrock areas within exposed metamorphic terraines such as the central highland areas within the Kabul Basin and the younger (least weathered) alluvial fans and felsic-gneiss bedrock source areas to the west (fig. 12A; Bohannon and Turner, 2007).

Analysis of VNIR-SWIR image spectra throughout the Kabul Basin and surrounding areas suggests that aluminous-clays with prominent 2.2 μm absorptions are widespread and ubitiquous throughout the basin-fill sediments and bedrock source areas. However, the Dez Sabz subbasin appears to contain the most abundant amounts of smectite clays such as montmorillonite (white-colored areas, fig. 7-2B). Smectites are shrink-swell clays that tend to form in areas of poor-drainage, commonly resulting in impermeable soils and groundwater aquitards in buried sediments. Smectite clays also appear abundant in the eastern portions of the Central Kabul subbasin, western portions of the Paghman and Upper Kabul subbasin, and southernmost portions of the Shomali subbasin (fig. 7-2B). These areas all correspond with areas that appear bright white in the false-colored composite of ASTER bands 6, 3 and 1 shown in figure 7-1B.

Biotite- and (or) chlorite-bearing areas (white- and red-colored areas, fig. 7-2C) generally correspond well with areas containing abundant ferrous-iron minerals based on band-ratios (red- and white-colored areas, fig. 7-1D), though the former shows better detail and resolves talus deposits associated with the main bedrock outcrop source areas. Notably, biotite-rich metamorphic rocks are exposed in the bedrock highland areas of the central parts of the Kabul Basin (Bohannon and Turner, 2007). Chlorite is a major constituent of serpentinized mafic- and ultramafic rocks and can also occur as a weathering product of biotite. Both minerals have broadly similar spectral shapes, but chlorite has a considerably stronger Mg-OH absorption feature near 2.33 μm and a stronger ferrous iron (Fe^{2+}) slope near 1.00 μm (Rowan and others, 2005). Chlorite of the first type (serpentization) is most likely responsible for the white-colored abundant levels (fig. 7-2C) covering least-weathered parts of the ophiolite deposit exposed to the northeast of the Kabul Basin. The presence of smectite absorption features in biotite and (or) chlorite-rich areas suggest that these rocks may have undergone considerable weathering, even in areas closest to the bedrock source where we expect the freshest exposures to occur. Except for talus deposits adjacent to their source bedrock outcrops, the basin-fill deposits appear to be depleted in chlorite and (or) biotite (fig. 7-2C), which agrees with the corresponding ferrous-iron ratio abundance maps (fig. 7-1D).

Illite and muscovite are common constituents of K-rich rocks and sediments. Illite is a clay mineral, typically of detrital origin, which is commonly derived from the weathering of mica-rich rocks. Both minerals have similar and nearly indistinguishable absorption features in hyperspectral data (Zhang and others, 2001), which become even less distinguishable when resampled to the SWIR multispectral resolution of ASTER (Rowan and others, 2005). Although the most common varieties of illite and muscovite share prominent 2.22 μm absorption features with smectite, they can be distinguished on the basis of secondary absorption features near 2.33 μm (Rowan and others, 2005). The areas containing the most abundant amounts of illite and (or) muscovite (white-colored areas, fig. 7-2D) correspond with many of the bedrock areas containing the most abundant quartz (white-colored areas, fig. 7-1C). These areas are mapped as Proterozoic mica-bearing gneisses and schists, Pliocene-age clastic sedimentary rocks, and Quaternary-age shingly and detrital sediments (Bohannon and Turner, 2007). In fact, prominent bedding-like structure displayed in several of these white-colored bedrock areas (fig. 7-2D) suggest that they may be highlighting foliation structure within mica-schist members of these Proterozoic rocks. Smaller, circular-shaped bedrock areas containing abundant illite and (or) muscovite could be related to unmapped intrusive rocks and (or) associated hydrothermal alteration. With the possible exception of the northwestern portion of the Shomali subbasin, much of the basin-fill sediments of the Kabul Basin appear to contain relatively lower abundances of illite and (or) muscovite (fig. 7-2D). Dry vegetation and carbonates share an overlapping absorption feature with illite at 2.33 μm, such that mixtures of smectite with either or both carbonate and dry vegetation material can resemble illite and (or) muscovite. Therefore, because the northwestern parts of the Shomali subbasin contain abundant carbonate (figs. 7-1A and 7-2E) as well as extensively cultivated vegetation (fig. 2-1B), these areas with apparently high illite and (or) muscovite abundance levels could be the result of abundant smectite rather than illite or muscovite (figs. 7-2B and D).

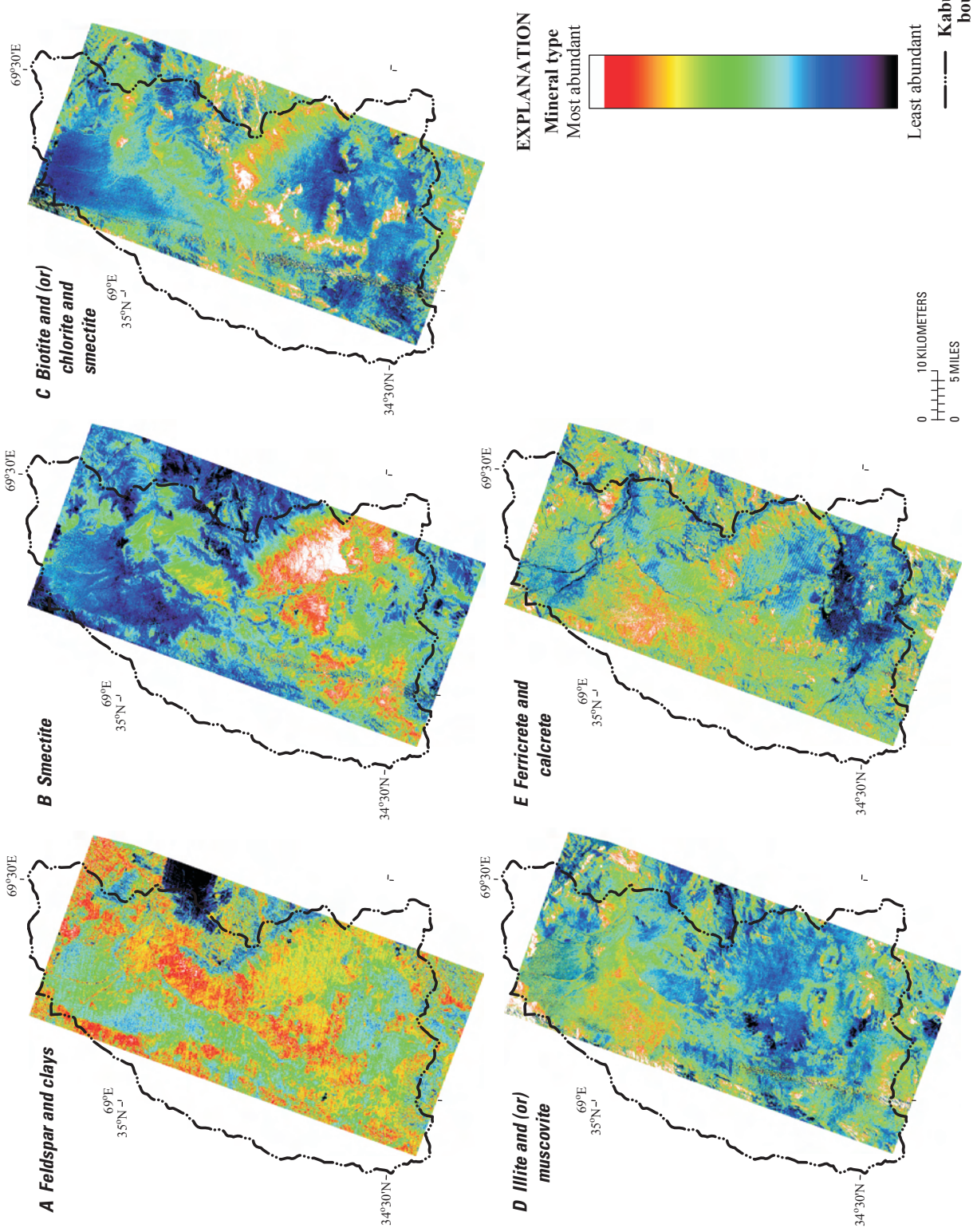

Figure 7-2. ASTER analysis of relative abundance of mineral groups containing (A) feldspar and clays, (B) smectite clays, (C) biotite and (or) chlorite and smectite, (D) illite and (or) muscovite, and (E) ferricrete and calcrete minerals in the Kabul Basin, Afghanistan. (This figure is the same as figure 12 on page 25 in the report)

With the exception of the built-up areas in and around the city of Kabul, basin-fill deposits of the Kabul Basin contain abundant carbonate minerals (red-colored areas, fig. 7-1A) and ferric-iron minerals (red-colored areas, fig. 7-1E) as noted earlier using TIR and VNIR-SWIR band-ratios. Spectral matched-filter processing suggests that the areas containing the most abundant ferricrete and calcrete deposits, of perhaps hardpan origin, are the northwestern portion of the Shomali subbasin, several of the alluvial fans derived from middle Triassic carbonate-bearing bedrock source areas to the northeast of the Dez Sabz subbasin, and sizeable patches of the Logar subbasin that are clearly distinguishable from bedrock (fig. 7-2E). However, the areas displaying the highest levels of abundance (white-colored areas, fig. 7-2E) of this hardpan (or alluvial?) mixture lay outside of the Kabul Basin. Several of these are limestone bedrock exposures of Cambrian-age and mineralized areas along the Herat suture-zone to the northwest of the basin (Bohannon and Turner, 2007). Other notable areas are within the ophiolite complex northeast of the Kabul Basin, which exposes serpentinized and weathered ultramafic rocks containing abundant chlorite and ferric-iron minerals (figs. 7-2C and 7-1E, respectively). Because chlorite share a prominent absorption feature at 2.33 μm with calcite, the two minerals can easily be confused and mis-identified using solely ASTER VNIR-SWIR data without the additional information provided using the ASTER TIR bands (Dalton and others, 2004; Rowan and others, 2005).

References Cited

Boardman, J.W., Kruse, F.A., and Green, R.O., 1995, Mapping target signatures via partial unmixing of AVIRIS data *in* Proceedings of the fifth JPL airborne earth science workshop, January 23–26: Pasadena, Calif., JPL Publication 95–01, p. 23–26.

Bohannon, R.G., and Turner, K.J., 2007, Geologic map of quadrangle 3468, Chak Wardak-Syahgerd (509) and Kabul (510) quadrangles, Afghanistan: U.S. Geological Survey Open-File Report 2005–1107–A. 1 sheet.

Dalton, J.B., Bove, D.J., Mladinich, C.S., and Rockwell, B.W., 2004, Identification of spectrally similar materials using the USGS Tetracorder algorithm—The calcite-epidote-chlorite problem: Remote Sensing of Environment, v. 89, p. 455–466.

Green, A.A., Berman, M., Switzer, B., and Craig, M.D., 1988, A transformation for ordering multispectral data in terms of image quality with implications for noise removal: IEEE Transactions on Geoscience and Remote Sensing, v. 26, no. 1, p. 65–74.

Harsanyi, J.C., and Chang, C., 1994, Hyperspectral image classification and dimensionality reduction—An orthogonal subspace projection approach: IEEE Transactions on Geoscience and Remote Sensing, v. 32, no. 4, p. 779–785.

Hewson, R.D., Cudahy, T.J., Mizuhiko, S., Ueda, K., and Mauger, A.J., 2005, Seamless geological map generation using ASTER in the Broken Hill-Curnamona province of Australia: Remote Sensing of Environment, v. 99, p. 159–172.

Kahle, A.B., Gillespie, A.R., Abbott, E.A., Abrams, M.J., Walker, R.E., and Gordon, H., 1988, Relative dating of Hawaiian lava flows using multispectral thermal infrared images—A new tool for geologic mapping of young volcanic terranes: Journal of Geophysical Research, v. 93, no. B12, p. 15239–15251.

Kruse, F.A., Lefkoff, A.B., Boardman, J.W., Heidebrecht, K.B., Shapiro, A.T., Barloon, P.J., and Goetz, A.F.H., 1993, The Spectral Image Processing System (SIPS)–Interactive visualization and analysis of imaging spectrometer data: Remote Sensing of Environment, v. 44, p. 145–163.

Ninomiya, Y., Fu, B., and Cudahy, T.J., 2005, Detecting lithology with Advanced Spaceborne Thermal Emission and Reflection Radiometer (ASTER) multispectral thermal infrared "radiance-at-sensor" data: Remote Sensing of Environment, v. 99, p. 127–139.

Rowan, L.C., and Mars, J.C., 2003, Lithologic mapping in the Mountain Pass, California area using Advanced Spaceborne Thermal Emission and Reflection Radiometer (ASTER) data: Remote Sensing of Environment, v. 84, p. 350–366.

Rowan, L.C., Mars, J.C., and Simpson, C.J., 2005, Lithologic mapping of the Mordor, NT, Australia ultramafic complex by using the Advanced Spaceborne Thermal Emission and Reflection Radiometer (ASTER): Remote Sensing of Environment, v. 99, p. 105–126.

Zhang, G., Wasyliuk, K., and Pan, Y., 2001, The characterization and quantitative analysis of clay minerals in the Athabasca Basin, Saskatchewan—Application of shortwave infrared reflectance spectroscopy: The Canadian Mineralogist, v. 39, p. 1347–1363.

This page intentionally left blank.

Appendix 8. Surface-Water Analysis

Contents

Tables

Appendix 8. Surface-Water Analysis

The probabilities of occurrence of annual high discharges are presented in table 8-1 for the 12 streamgages. Probability of occurrence is an estimate of the likelihood that a particular discharge in a stream will be equaled or exceeded in a given year. The probability of occurrence of a high flow is called the exceedance probability. For example, the maximum instantaneous discharge for the 0.20 exceedance probability is listed as 56.2 m^3/s for Kabul River at Tang-i-Saidan, then a 20 percent chance exists that a discharge equal to or greater than 56.2 m^3/s will occur once during the year. Recurrence interval is another way of expressing annual probability and is the reciprocal of probability of occurrence. For example, the recurrence interval for an exceedance probability of 0.20 is 5 years (1 divided by 0.20). For a long discharge record, the annual maximum discharge can be expected to equal or exceed that discharge on average once every 5 years.

The maximum instantaneous discharge and the maximum mean discharge for 3, 7, 15, and 30 consecutive-day periods for selected exceedance probabilities and recurrence intervals are listed in table 8-1. Values for the maximum mean discharges for 3, 7, 15, and 30 consecutive-day periods are computed from the annual high mean values of the corresponding periods. The computations are based on the log-Pearson Type III distribution using values obtained for the water year. The difference in percent between the maximum instantaneous discharge and a maximum mean discharge for a "n" consecutive-day period can be used as an indicator of the flashiness of a flood. As an example, the mean discharge for a 3 consecutive-day period for a recurrence interval of 25 years for streamgages Qargha River above Qargha Reservior and Paghman River at Pul-i-Sokhta are 72 and 77 percent, respectively; the recurrence intervals for the rest of the streamgages are from 11 to 32 percent. Therefore, the high flows are much shorter duration (flashier) at the streamgages Qargha River above Qargha Reservior and Paghman River at Pul-i-Sokhta than at the other streamgages.

The annual peak discharges for each of the 12 streamgages are listed in table 8-2. The recurrence intervals for the peak discharge for the period of record are 10 years for streamgage at Shatul River at Gulbahar; 10–25 years for streamgages Qargha River above Qargha Reservoir, Qargha River below Qargha Reservoir, Paghman River at Pul-i-Sokhta, Logar River at Sang-i-Naweshta, Kabul River at Tang-i-Gharu, Panjsher River at Gulbahar, and Panjsher River at Shukhi; 25 years for streamgages Chakari River at Band-i-Amir Ghazi, Kabul River at Tang-i-Saidan, and Ghorband River at Pul-i-Ashawa; and 50 years for streamgage Salang River at Bagh-i-Lala. The instantaneous peak discharge of 192 m^3/s was on April 28, 1967, for streamgage Kabul River at Tang-i-Gharu, and the instantaneous peak discharge of 750 m^3/s was on June 12, 1967, for the streamgage Panjsher River at Shukhi.

The annual low discharge in any given year is sensitive to natural-channel processes, such as evapotranspiration and groundwater gains and losses, and human-induced hydrologic modifications, such as the operation of many small water-storage reservoirs; the effects of surface-water withdrawal for agricultural, municipal, and industrial use; and the effects of return flow to the river. The probabilities of occurrence of annual low discharges are presented in table 8-3 for the 12 streamgages. Probability of occurrence is an estimate of the likelihood that a particular discharge in a stream will be equaled or exceeded in 1 year or, in the case of low flows, the likelihood that the discharge will not be equaled or exceeded during the year. The probability of occurrence of low flow is called the nonexceedance probability. The table of probability of occurrence of annual low discharges for each streamgage lists the minimum mean discharge for 1, 3, 7, 14, 30, and 60 consecutive-day periods for selected nonexceedance probabilities and recurrence intervals. Values for the minimum mean discharges are computed from the annual low discharge values of the corresponding periods using the log-Pearson Type III distribution. Probabilities of annual low discharges are computed using values for the climatic year (April 1 through March 31).

Table 8-1. Probability of occurrence of annual high discharge for the period of record at streamflow-gaging stations in the Kabul study area, Afghanistan.

[m^3/s, cubic meters per second]

Exceedance probability	Recurrence interval (years)	Maximum instantaneous (m^3/s)	Maximum mean discharge (m^3/s)			
			3-day period	7-day period	15-day period	30-day period
Kabul River at Tangi Saidan						
0.99	1.01	7.4	5.40	4.08	3.44	2.73
0.95	1.05	12.5	8.40	6.93	6.04	4.94
0.90	1.11	16.3	10.60	9.08	8.01	6.63
0.80	1.25	21.9	14.10	12.40	11.10	9.29
0.50	2	36.3	24.30	22.00	19.70	16.70
0.20	5	56.2	41.70	37.10	32.80	28.00
0.10	10	68.7	55.20	48.00	41.90	35.70
0.04	25	83.4	74.40	62.30	53.50	45.30
0.02	50	93.6	90.20	73.30	62.00	52.30
0.01	100	103.0	107.00	84.40	70.40	59.10
Qargha River above Qargha Reservoir						
0.99	1.01	1.7	1.51	1.31	1.03	0.90
0.95	1.05	2.3	1.94	1.65	1.33	1.13
0.90	1.11	2.7	2.20	1.87	1.52	1.27
0.80	1.25	3.2	2.54	2.17	1.79	1.48
0.50	2	4.2	3.32	2.88	2.47	2.00
0.20	5	5.3	4.26	3.83	3.43	2.73
0.10	10	5.9	4.81	4.44	4.08	3.23
0.04	25	6.6	5.45	5.20	4.93	3.89
0.02	50	7.0	5.89	5.76	5.57	4.39
0.01	100	7.3	6.30	6.32	6.23	4.90
Qargha River below Qargha Reservoir						
0.99	1.01	0.4	0.35	0.32	0.29	0.25
0.95	1.05	0.4	0.37	0.34	0.32	0.28
0.90	1.11	0.4	0.38	0.36	0.34	0.30
0.80	1.25	0.5	0.42	0.40	0.37	0.33
0.50	2	0.7	0.54	0.53	0.49	0.43
0.20	5	1.3	0.87	0.82	0.72	0.62
0.10	10	2.1	1.22	1.11	0.92	0.79
0.04	25	4.0	1.87	1.62	1.26	1.05
0.02	50	6.5	2.59	2.14	1.58	1.28
0.01	100	10.6	3.56	2.82	1.97	1.56

Table 8-1. Probability of occurrence of annual high discharge for the period of record at streamflow-gaging stations in the Kabul study area, Afghanistan.—Continued

[m^3/s, cubic meters per second]

Exceedance probability	Recurrence interval (years)	Maximum instantaneous (m^3/s)	Maximum mean discharge (m^3/s)			
			3-day period	7-day period	15-day period	30-day period
Paghman River at Pul-i-Sokhta						
0.99	1.01	1.8	0.89	0.63	0.45	0.39
0.95	1.05	3.4	1.70	1.25	0.96	0.79
0.90	1.11	4.7	2.37	1.79	1.41	1.14
0.80	1.25	7.2	3.50	2.71	2.20	1.73
0.50	2	16.0	7.13	5.81	4.78	3.65
0.20	5	35.6	13.9	11.9	9.57	7.18
0.10	10	54.3	19.4	17.0	13.3	9.95
0.04	25	85.0	27.2	24.5	18.5	13.8
0.02	50	114.0	33.7	30.8	22.7	16.9
0.01	100	148.0	40.6	37.6	27.0	20.1
Logar River at Sang-i-Naweshta						
0.99	1.01	16.1	13.0	13.3	12.3	11.2
0.95	1.05	22.0	18.0	17.3	15.5	13.7
0.90	1.11	26.0	21.4	20.0	17.8	15.5
0.80	1.25	31.7	26.3	24.0	21.0	18.0
0.50	2	46.0	39.1	34.8	29.9	25.0
0.20	5	66.4	48.0	42.4	36.4	30.0
0.10	10	80.3	58.2	51.4	44.1	36.1
0.04	25	98.0	71.6	63.8	54.7	44.4
0.02	50	111.0	89.4	80.8	69.7	56.4
0.01	100	125.0	103.0	94.5	82.1	66.2
Chakari River at Band-i-Amir Ghazi						
0.99	1.01	0.3	0.27	0.27	0.25	0.24
0.95	1.05	0.4	0.39	0.39	0.36	0.34
0.90	1.11	0.5	0.47	0.47	0.44	0.42
0.80	1.25	0.7	0.59	0.59	0.55	0.52
0.50	2	1	0.9	0.89	0.85	0.78
0.20	5	1.4	1.34	1.32	1.27	1.14
0.10	10	1.7	1.64	1.62	1.55	1.38
0.04	25	2	2.02	1.99	1.92	1.67
0.02	50	2.2	2.31	2.27	2.19	1.89
0.01	100	2.4	2.59	2.55	2.46	2.1

Table 8-1. Probability of occurrence of annual high discharge for the period of record at streamflow-gaging stations in the Kabul study area, Afghanistan.—Continued

[m^3/s, cubic meters per second]

Exceedance probability	Recurrence interval (years)	Maximum instantaneous (m^3/s)	Maximum mean discharge (m^3/s)			
			3-day period	7-day period	15-day period	30-day period
Kabul River at Tangi-Gharu						
0.99	1.01	27.4	16.2	15.0	12.6	11.6
0.95	1.05	41.5	26.4	23.9	20.4	18.2
0.90	1.11	51.0	33.8	30.4	26.1	22.9
0.80	1.25	64.8	45.1	40.3	35.0	30.1
0.50	2	98.3	75.4	67.9	59.6	50.1
0.20	5	142.0	121.0	111.0	97.9	81.6
0.10	10	169.0	152.0	142.0	125.0	104.0
0.04	25	201.0	192.0	184.0	161.0	135.0
0.02	50	223.0	221.0	215.0	189.0	158.0
0.01	100	244.0	250.0	247.0	217.0	183.0
Panjsher River at Gulbahar						
0.99	1.01	209	179	166	146	125
0.95	1.05	255	209	193	172	152
0.90	1.11	282	227	210	188	168
0.80	1.25	318	250	232	209	189
0.50	2	394	300	281	257	234
0.20	5	483	360	343	317	286
0.10	10	534	395	381	353	316
0.04	25	592	436	427	398	349
0.02	50	631	465	460	429	372
0.01	100	668	492	492	460	393
Shatul River at Gulbahar						
0.99	1.01	16.1	9.47	8.86	8.20	7.06
0.95	1.05	19.2	11.90	11.20	10.30	9.10
0.90	1.11	21.2	13.40	12.60	11.70	10.40
0.80	1.25	23.7	15.40	14.50	13.40	12.10
0.50	2	29.5	19.80	18.60	17.50	15.90
0.20	5	36.7	25.00	23.60	22.40	20.60
0.10	10	41.1	28.00	26.60	25.40	23.40
0.04	25	46.4	31.50	30.00	28.90	26.70
0.02	50	50.2	33.90	32.40	31.30	28.90
0.01	100	53.9	36.10	34.60	33.70	31.00

Table 8-1. Probability of occurrence of annual high discharge for the period of record at streamgages in the Kabul study area, Afghanistan.—Continued

[m^3/s, cubic meters per second]

Exceedance probability	Recurrence interval (years)	Maximum instantaneous (m^3/s)	Maximum mean discharge (m^3/s)			
			3-day period	7-day period	15-day period	30-day period
Ghorband River at Pul-i-Ashawa						
0.99	1.01	55.0	48.0	44.4	41.5	38.3
0.95	1.05	67.0	57.1	53.0	49.6	45.7
0.90	1.11	74.2	62.6	58.3	54.6	50.3
0.80	1.25	83.7	70.0	65.5	61.2	56.4
0.50	2	104.0	86.8	81.8	76.3	70.3
0.20	5	129.0	107.0	102.0	94.9	87.7
0.10	10	143.0	120.0	115.0	106.0	98.4
0.04	25	159.0	135.0	131.0	120.0	111.0
0.02	50	170.0	146.0	142.0	130.0	120.0
0.01	100	180.0	157.0	152.0	139.0	130.0
Salang River at Bagh-i-Lala						
0.99	1.01	18.9	11.9	10.7	10.1	9.79
0.95	1.05	26.8	17.7	16.7	16.0	15.1
0.90	1.11	32.0	21.6	20.6	19.7	18.5
0.80	1.25	39.4	27.1	26.0	24.7	22.9
0.50	2	57.2	40.1	37.7	34.8	31.8
0.20	5	80.6	56.2	50.3	44.4	40.2
0.10	10	95.2	65.8	56.7	48.6	44.0
0.04	25	113.0	76.7	63.1	52.4	47.3
0.02	50	125.0	84.1	66.9	54.3	49.1
0.01	100	137.0	90.9	70.1	55.8	50.4
Panjsher River at Shukhi						
0.99	1.01	318	248	227	200	178
0.95	1.05	375	296	273	242	215
0.90	1.11	408	325	300	267	238
0.80	1.25	453	362	336	300	268
0.50	2	548	440	412	374	338
0.20	5	659	528	499	462	424
0.10	10	724	578	549	514	477
0.04	25	798	633	605	575	541
0.02	50	849	671	644	618	586
0.01	100	897	705	679	658	630

Table 8-2. Annual peak discharge for streamgages in the Kabul study area for the period of record.

[m^3/s, cubic meters per second]

Water year	Date	Peak discharge (m^3/s)	Water year	Date	Peak discharge (m^3/s)
Kabul River at Tangi Saidan					
1962	April 20, 1962	25.7	1972	April 28, 1972	58.2
1963	May 4, 1963	30.7	1973	April 11, 1973	47.0
1964	April 12, 1964	34.3	1974	April 7, 1974	18.5
1965	April 23, 1965	37.4	1975	April 4, 1975	32.0
1966	April 27, 1966	21.8	1976	April 24, 1976	65.6
1967	April 27, 1967	87.2	1977	May 27, 1977	28.4
1968	April 30, 1968	57.8	1978	July 6, 1978	57.8
1969	April 15, 1969	32.2	1979	August 7, 1979	35.5
1970	April 26, 1970	11.5	1980	April 19, 1980	60.8
1971	March 26, 1971	10.8			
Qargha River above Qargha Reservoir					
1963	May 12, 1963	3.34	1974	March 21, 1974	5.60
1964	May 8, 1964	4.31	1975	April 4, 1975	3.50
1965	April 21, 1965	3.30	1976	April 22, 1976	4.00
1966	April 24, 1966	6.15	1977	April 15, 1977	3.55
1970	May 1, 1970	4.80	1978	July 6, 1978	5.00
1971	April 16, 1971	2.50	1979	May 19, 1979	4.10
1972	April 7, 1972	5.25	1980	April 5, 1980	6.11
1973	April 2, 1973	2.08			
Qargha River below Qargha Reservoir					
1965	May 11, 1965	1.27	1973	July 18, 1973	0.70
1966	August 22, 1966	0.44	1974	October 1973	0.60
1967	June 18, 1967	0.58	1975	August 21, 1975	0.55
1968	May 2, 1968	1.20	1976	May 18, 1976	0.65
1969	June 1, 1969	0.93	1977	October 18, 1976	0.45
1970	June 20, 1970	0.63	1978	July 3, 1978	3.06
1971	June 7, 1971	0.50	1979	July 11, 1979	0.56
1972	May 14, 1972	5.90	1980	October 1, 1979	0.48
Paghman River at Pul-i-Sokhta					
1963	May 12, 1963	17.80	1972	May 6, 1972	19.50
1964	April 10, 1964	15.50	1973	August 2, 1973	17.10
1965	May 7, 1965	16.00	1974	April 7, 1974	10.50
1966	April 27, 1966	5.56	1975	August 13, 1975	80.00
1967	April 27, 1967	34.80	1976	April 27, 1976	13.10
1968	April 30, 1968	48.80	1977	April 10, 1977	7.40
1969	April 19, 1969	4.65	1978	August 17, 1978	70.50
1970	July 7, 1970	4.00	1979	March 29, 1979	39.20
1971	April 12, 1971	3.42	1980	April 11, 1980	23.70

Table 8-2. Annual peak discharge for streamgages in the Kabul study area for the period of record.—Continued

[m^3/s, cubic meters per second]

Water year	Date	Peak discharge (m^3/s)	Water year	Date	Peak discharge (m^3/s)
Logar River at Sang-i-Naweshta					
1962	March 31, 1962	36.60	1972	April 28, 1972	58.60
1963	May 13, 1963	52.90	1973	April 13, 1973	62.00
1964	April 13, 1964	65.30	1974	April 8, 1974	41.20
1965	April 25, 1965	85.00	1975	April 5, 1975	40.00
1966	April 14, 1966	27.90	1976	April 27, 1976	57.60
1967	April 28, 1967	95.00	1977	May 28, 1977	28.10
1968	April 9, 1968	36.00	1978	July 9, 1978	88.00
1969	April 20, 1969	34.00	1979	April 14, 1979	45.30
1970	November 12, 1969	25.30	1980	April 19, 1980	53.50
1971	March 26, 1971	19.70			
Chakari River at Band-i-Amir Ghazi					
1965	July 5, 1965	1.46	1973	April 21, 1973	0.55
1966	May 1, 1966	1.00	1974	June 8, 1974	1.06
1967	May 23, 1967	1.26	1975	October 23, 1974	0.39
1968	December 9, 1967	1.67	1976	May 7, 1976	0.82
1969	March 13, 1969	0.55	1977	August 9, 1977	0.82
1970	July 17, 1970	0.96	1978	June 9, 1978	1.19
1971	May 1, 1971	0.55	1979	September 13, 1979	1.43
1972	June 18, 1972	1.36	1980	April 17, 1980	1.92
Kabul River at Tangi-Gharu					
1960	May 2, 1960	175.0	1971	March 26, 1971	43.6
1961	April 18, 1961	98.0	1972	April 28, 1972	107.0
1962	November 15, 1961	39.5	1973	April 11, 1973	107.0
1963	May 19, 1963	165.0	1974	April 7, 1974	48.2
1964	April 10, 1964	158.0	1975	April 4, 1975	68.8
1965	April 25, 1965	156.0	1976	April 25, 1976	128.0
1966	April 26, 1966	79.7	1977	April 18, 1977	47.4
1967	April 28, 1967	192.0	1978	July 7, 1978	109.0
1968	April 30, 1968	115.0	1979	April 14, 1979	69.5
1969	April 19, 1969	85.5	1980	April 19, 1980	107.0
1970	July 7, 1970	101.0			
Panjsher River at Gulbahar					
1960	July 10, 1960	584	1971	June 9, 1971	321
1961	June 5, 1961	515	1972	June 25, 1972	385
1962	June 10, 1962	488	1973	June 13, 1973	473
1963	June 20, 1963	520	1974	June 16, 1974	292
1964	July 4, 1964	569	1975	June 17, 1975	335
1965	July 15, 1965	300	1976	June 4, 1976	327
1966	June 19, 1966	335	1977	June 23, 1977	338
1967	June 12, 1967	358	1978	June 5, 1978	418

Table 8-2. Annual peak discharge for streamgages in the Kabul study area for the period of record.—Continued

[m3/s, cubic meters per second]

Water year	Date	Peak discharge (m^3/s)	Water year	Date	Peak discharge (m^3/s)
Panjsher River at Gulbahar—Continued					
1968	July 8, 1968	412	1979	June 23, 1979	477
1969	June 20, 1969	424	1980	June 9, 1980	220
1970	June 3, 1970	350			
Shatul River at Gulbahar					
1967	June 11, 1967	41.8	1974	June 4, 1974	21.6
1968	June 25, 1968	41.8	1975	June 17, 1975	30.9
1969	June 16, 1969	28.2	1976	July 6, 1976	24.5
1970	May 21, 1970	27.6	1977	June 22, 1977	20.7
1971	May 19, 1971	20.6	1978	June 5, 1978	27.0
1972	June 12, 1972	40.6	1979	June 13, 1979	35.0
1973	June 11, 1973	35.1			
Ghorband River at Pul-i-Ashawa					
1960	April 18, 1960	146.0	1970	May 21, 1970	73.2
1961	June 5, 1961	139.0	1971	May 20, 1971	69.7
1962	June 11, 1962	84.4	1972	June 13, 1972	123.0
1963	May 15, 1963	96.2	1973	June 4, 1973	111.0
1964	April 11, 1964	93.0	1974	June 1, 1974	63.2
1965	June 13, 1965	118.0	1975	May 16, 1975	121.0
1966	June 18, 1966	108.0	1976	June 4, 1976	130.0
1967	April 27, 1967	161.0	1977	May 27, 1977	86.4
1968	June 10, 1968	131.0	1978	April 17, 1978	85.6
1969	June 17, 1969	97.5	1979	June 22, 1979	96.8
Salang River at Bagh-i-Lala					
1962	April 25, 1962	43.8	1972	May 13, 1972	80.8
1963	May 14, 1963	92.8	1973	June 3, 1973	56.7
1965	June 13, 1965	50.0	1974	May 1, 1974	45.5
1966	April 25, 1966	60.6	1975	May 15, 1975	60.0
1967	April 27, 1967	124.0	1976	April 23, 1976	53.1
1968	April 29, 1968	76.1	1977	May 27, 1977	27.9
1969	April 14, 1969	91.0	1978	April 17, 1978	41.6
1970	April 15, 1970	58.5	1979	April 30, 1979	48.9
1971	May 19, 1971	22.4			
Panjsher River at Shukhi					
1967	June 12, 1967	750	1974	June 18, 1974	380
1968	June 25, 1968	680	1975	June 17, 1975	451
1969	June 20, 1969	626	1976	June 4, 1976	482
1970	June 3, 1970	509	1977	June 23, 1977	392
1971	May 28, 1971	522	1978	July 7, 1978	590
1972	June 28, 1972	719	1979	June 22, 1979	558
1973	June 13, 1973	700	1980	June 9, 1980	452

Table 8-3. Probability of occurrence of annual low discharge for the period of record at streamgages in the Kabul study area.

[m^3/s, cubic meters per second]

Nonexceedance probability	Recurrence interval (years)	Minimum mean discharge (m^3/s)					
		Number of consecutive days					
		1	3	7	14	30	60
Kabul River at Tangi Saidan							
0.05	20	0.000	0.009	0.017	0.045	0.073	0.089
0.10	10	0.008	0.017	0.029	0.060	0.093	0.115
0.20	5	0.023	0.033	0.052	0.084	0.124	0.153
0.50	2	0.089	0.104	0.135	0.159	0.208	0.254
Qargha River above Qargha Reservoir							
0.05	20	0.023	0.023	0.023	0.023	0.023	0.025
0.10	10	0.024	0.025	0.025	0.025	0.026	0.029
0.20	5	0.027	0.028	0.029	0.029	0.031	0.036
0.50	2	0.034	0.035	0.037	0.040	0.044	0.053
Paghman River at Pul-i-Sokhta							
0.05	20	0.000	0.000	0.000	0.000	0.000	0.000
0.10	10	0.000	0.000	0.000	0.000	0.000	0.004
0.20	5	0.000	0.003	0.006	0.006	0.007	0.008
0.50	2	0.012	0.013	0.015	0.017	0.021	0.026
Logar River at Sang-i-Naweshta							
0.05	20	0.000	0.000	0.000	0.004	0.009	0.020
0.10	10	0.000	0.005	0.008	0.008	0.016	0.034
0.20	5	0.012	0.014	0.018	0.019	0.033	0.063
0.50	2	0.068	0.069	0.077	0.096	0.124	0.205
Chakari River at Band-i-Amir Ghazi							
0.05	20	0.000	0.000	0.000	0.008	0.009	0.01
0.10	10	0.007	0.007	0.007	0.009	0.01	0.012
0.20	5	0.009	0.009	0.009	0.011	0.013	0.015
0.50	2	0.014	0.014	0.014	0.015	0.02	0.025
Kabul River at Tangi-Gharu							
0.05	20	0.000	0.000	0.013	0.018	0.021	0.045
0.10	10	0.011	0.012	0.022	0.030	0.037	0.069
0.20	5	0.028	0.031	0.043	0.057	0.069	0.115
0.50	2	0.112	0.125	0.141	0.181	0.217	0.316

Table 8-3. Probability of occurrence of annual low discharge for the period of record at streamgages in the Kabul study area.—Continued

[m^3/s, cubic meters per second]

Nonexceedance probability	Recurrence interval (years)	Minimum mean discharge (m^3/s)					
		Number of consecutive days					
		1	3	7	14	30	60
Panjsher River at Gulbahar							
0.05	20	6.39	6.47	6.58	6.72	6.85	7.20
0.10	10	6.88	7.00	7.14	7.28	7.44	7.78
0.20	5	7.53	7.69	7.85	8.01	8.19	8.53
0.50	2	8.91	9.14	9.33	9.51	9.75	10.10
Shatul River at Gulbahar							
0.05	20	0.006	0.006	0.007	0.100	0.011	0.016
0.10	10	0.007	0.007	0.009	0.012	0.014	0.020
0.20	5	0.009	0.010	0.012	0.015	0.019	0.027
0.50	2	0.018	0.019	0.023	0.030	0.038	0.053
Ghorband River at Pul-i-Ashawa							
0.05	20	3.27	3.34	3.43	3.57	3.76	4.12
0.10	10	3.80	3.89	3.99	4.15	4.39	4.80
0.20	5	4.54	4.65	4.76	4.95	5.23	5.69
0.50	2	6.26	6.44	6.58	6.78	7.10	7.62
Salang River at Bagh-i-Lala							
0.05	20	1.28	1.54	1.58	1.63	1.73	1.86
0.10	10	1.41	1.66	1.70	1.75	1.86	1.99
0.20	5	1.59	1.81	1.87	1.92	2.03	2.17
0.50	2	2.00	2.17	2.25	2.30	2.41	2.55
Panjsher River at Shukhi							
0.05	20	20.7	20.9	21.2	21.5	21.8	23.0
0.10	10	21.6	21.8	22.0	22.4	22.8	24.0
0.20	5	22.7	22.8	23.1	23.4	23.9	25.2
0.50	2	24.8	24.9	25.1	25.4	26.2	27.5

This page intentionally left blank.

Appendix 9. Groundwater Levels

Contents

Appendix 9. Groundwater Levels

Groundwater-level conditions in the Logar, Central Kabul, Deh Sabz, Paghman and Upper Kabul, and Shomali subbasins are discussed below with references to historical conditions where possible. Groundwater-level hydrographs for the subbasins of the Kabul Basin are provided by Akbari and others (2007). Monthly groundwater data do not exist for the Panjsher River subbasin; however, conditions are likely to be similar to the northernmost parts of the Shomali subbasin where the aquifer is influenced by Panjsher River losses.

Logar Subbasin

The depth to water on the western bank of the Logar River (Logar aquifer) is reported to be between 30 to 80 centimeters (cm) in the lower flat-lying area and between 1.5 and 2 meters (m) in the higher regions (elevations) during the period of investigation (2003–2005). Böckh (1971) reported that the water levels on the eastern bank of the Logar River ranged from around 5 to 10 m below land surface and that the depth to water fluctuated between 1 and 2 m in response to pumping for irrigation. The large difference between the depth to water on the west and east banks of the Logar River were attributed to differences in land-surface elevation. The Kabul aquifer generally has depths to water that range from 2 to 12 m and water-level fluctuations up to 5 m. Water levels in 1965 were from 2 to 5 m below land surface. The depth to water in the Paghman aquifer is very shallow near the center of the basin and increases towards the valley sides. Depth-to-water measurements made in 1962–1963 indicate a water level of 19 m below land surface near the confluence of the Cheltan and Paghman streams.

The Logar subbasin includes urban population centers and rural, agricultural land. Nine monitoring wells in the Logar subbasin ranged in total depth from 25 to 79.1 m. The surficial geology at the wells varied from Quaternary loess to Quaternary conglomerate and sandstone. Depth-to-water measurements under static conditions ranged from a minimum of 1.5 m (1,783.4 m above sea level) adjacent to the Logar River during May 2005 to a maximum of 10.2 m (1,781.1 m above sea level) during the fall of 2004 and 2006 at a well not in the vicinity of any streams or rivers. Seasonal water-level fluctuations from fall 2005 through spring 2006 ranged from about 1.3 to 4 m in the Logar subbasin. Water-level increases of up to 3.9 m from October 2004 until June 2006 were measured in a well along the Logar River. Many of the wells along the Logar River are municipal water-supply wells that are frequently pumped. Taking this into account, there does appear to be a strong seasonal recharge component that can be correlated to times of peak flow during winter and spring in the Logar River. Depth to water in one well rose from 9.3 m (1,783.3 m above sea level) in early January 2005 to 5 m (1,787.5 m above sea level) in May 2005. This change in water level corresponded to near-normal winter and spring precipitation and corresponding flow in the Logar River.

Central Kabul Subbasin

The Central Kabul subbasin includes the primary population center of Afghanistan (city of Kabul) in the western part of the subbasin and more rural lands in the eastern part of the subbasin. Twenty-four monitoring wells in the Central Kabul subbasin ranged in total depth from 6.6 to 160 m. One well was located on an outcrop of gneiss; at all other well sites, the surface geology consisted of Quaternary loess, fan alluvium and colluvium, or conglomerate and sandstone. Depth-to-water measurements under static conditions ranged from a minimum of about 2.5 m (1,790 m above sea level) during June 2005 to a maximum of about 23 m (1,778 m above sea level) during January and February 2006. Monitoring wells that have water levels not affected by pumping have seasonal fluctuations from 0.5 to 3 m. The water level in the supply well on the grounds of the Afghanistan Geological Survey building had a seasonal fluctuation of about 2 m. In general, it appears the wells near the Kabul River had increasing water levels during the monitoring period, and wells that are distant from the river had decreases in water level. The water-level summary plot for Well 208 shows a recovery of approximately 9 m from a dynamic water-level measurement in March 2005 to a static water-level measurement in early April 2005. The water-level measurement in this well in late April 2005 recorded a drop of about 8 m because of pumping. Larger water-level fluctuations caused by pumping were recorded in the Khair Khana wells; pumping-induced drawdown was up to 25 m.

Deh Sabz Subbasin

The Deh Sabz subbasin is a sparsely populated mixed agricultural and industrial area. Nine monitoring wells in the Deh Sabz subbasin ranged in depth from 7.2 to 150 m. The surficial geology at the wells varied from Quaternary loess to Quaternary conglomerate and sandstone. There are no perennial rivers or streams in this subbasin, although some ephemeral streams and some perennial springs discharge from the base of the mountains on the east side of this subbasin. Depth-to-water measurements under static conditions ranged from a minimum of 4 m (1,963.6 m above sea level) measured in early March 2007 to a maximum of 40 m (1,812.6 m above sea level) in August 2006. Seasonal water-level fluctuations ranged from 0.5 to 9 m. Seasonal water-level fluctuations are thought to be attributed to precipitation that falls locally on the valley floor or mountains to the east. Two wells in the Deh Sabz subbasin showed generally declining water levels during the monitoring period ranging from 0.9 m from April 2005 to September 2006 in one well and 1.0 m from August 2005 to May 2006 in another well.

The water level in a well that was 7.2 m deep increased approximately 3 m from August 2006 to March 2007. In a 150-m deep well, the static water level increased about 3 m from March 2005 to March 2007. The drawdown during

pumping in this well ranged from approximately 20 m to as much as 40 m. Recovery after pumping stopped was fairly rapid. The water-level elevation in mid-May 2006 under dynamic conditions was 1,784.6 m above sea level. The water-level elevation measured under static conditions in early June 2006 was 1,822.6 m above sea level, so the water level had increased about 38 m.

Paghman and Upper Kabul Subbasin

The Paghman and Upper Kabul subbasin includes the urban population centers of the western city of Kabul, and more rural agrarian lands in the western part of the subbasin. Twelve monitoring wells in the Paghman and Upper Kabul subbasin ranged in depth from 4.9 to 99.7 m. One well was located on an outcrop of gneiss; all other wells were in Quaternary loess, alluvium, or colluvium. Five of the monitoring wells are municipal water-supply wells. Three are located approximately 1 km west of the Kabul River near the confluence of the Kabul River and Paghman Stream. The other two are located much further west of the Kabul River and within a kilometer of the Paghman Stream. Depth-to-water measurements under static conditions ranged from 3 m (1,805.6 m above sea level) to 28 m (1,840.3 m above sea level). Seasonal water-level fluctuations from fall 2005 through spring 2006 ranged from about 0.5 to 3 m. The water levels in two wells declined from August 2004 until February 2007. One well declined about 3 m and the other about 8 m. These two wells were approximately 0.8 km apart and north of the Paghman Stream. Three wells had increases in water levels ranging from 3 to 5 m from February 2005 through March 2007. Only one municipal supply well had static water-level measurements spanning a fall-winter-spring precipitation cycle. Measurements under static conditions in this well from November 2004 until June 2005 showed an increase in the water level from 1,802.5 m above sea level to 1,804.6 m above sea level, an increase of 2.1 m. The water levels in wells close to the Kabul River had larger seasonal water-level increases than wells that are not near major surface-water sources.

Shomali Subbasin

The Shomali subbasin is a predominantly rural area that contains the largest irrigated agricultural area in the Kabul Basin. A number of springs discharge from the mountains on the western border of this subbasin. The flow from these springs is the source for a number of small perennial streams in the western part of the Shomali subbasin. The water in these streams is used for irrigation with much of the water being diverted to irrigation canals. As a result, these small streams eventually dry up and do not contribute flow to the Barik Ab River, the largest ephemeral stream in the subbasin. Fifteen monitoring wells in the Shomali subbasin ranged in depth from 9 to 102 m. The surficial geology at the well locations consisted of Quaternary loess or Quaternary fan alluvium and colluvium. The range of depth to water under static conditions was from 3.4 m below land surface in two wells (1,540 m above sea level in October 2005 and 1,877.7 m above sea level in May 2006) to 27.8 m below land surface (1,784.9 m above sea level) in August 2004. Seasonal water-level fluctuations ranged from approximately 0.5 to 8 m. The largest increase in the water level was approximately 13 m from 1,786.7 m above sea level in March 2005 to 1,799.7 m above sea level in May 2006. While the water level in most wells increased during the monitoring period, one well appeared to have an overall decline in water level from 1,644.4 m above sea level in late August 2004 to 1,642.9 m above sea level in October 2006. This decline may be attributed to pumping of the well before the October 2006 measurement. Two wells showed a steady increase in water levels during the monitoring period with minimal seasonal fluctuations. The seasonal high water levels in six wells increased with time and in three wells decreased with time. The deepest well in the monitoring network in the Shomali subbasin (102-m deep) had about a 0.5 m decline in water level between the July 2005 maximum and the late September 2005 minimum. The water level in this well increased during the monitoring period by about 8 m from 1,791.7 to 1,799.7 m above sea level. The water-level maximums in most wells were prior to mid-July, and in 2006 were prior to mid-June. Ephemeral streams in the Shomali subbasin are potential sources of recharge, especially during years when the Paghman Mountains receive near normal precipitation.

References Cited

Akbari, M.A., Tahir, M., Litke, D.W., and Chornack, M.P., 2007, Groundwater levels in the Kabul Basin, Afghanistan, 2004–07: U.S. Geological Survey Open-File Report 2007–1294, 46 p.

This page intentionally left blank.